Tampere University

Yekaterina Sadovaya

Resource Allocation and Multi-Connectivity Operation in Cellular IAB Networks

Faculty of Information Technology and Communication Sciences (ITC)
Master's thesis
August 2021

Abstract

Yekaterina Sadovaya: Resource Allocation and Multi-Connectivity Operation in Cellular IAB Networks
Master's thesis
Tampere University
Master's Degree Programme in Information Technology
August 2021
Examiners: Assoc. Prof. Sergey Andreev (Tampere University), Dr. Dmitri Moltchanov (Tampere University)
Supervisors: Assoc. Prof. Sergey Andreev (Tampere University), Dr. Dmitri Moltchanov (Tampere University), Dr. Hosein Nikopour (Intel Corporation)

The emerging 5G technology promises a capacity boost for future cellular networks due to the utilization of the millimeter-wave (mmWave) spectrum. However, radio propagation over mmWave bands implies higher propagation losses, resulting in reduced coverage for the 5G base station (gNB); thus, deployments become ultra-dense. Under the described conditions, using conventional wired backhaul may not be cost-efficient for network operators. Therefore, the concept of wireless backhaul is being considered by 3GPP, which is called integrated access and backhaul (IAB).

On the one hand, this technology allows the deployment cost to be reduced. On the other hand, wireless backhaul raises multiple challenges. This includes the half-duplex constraint, which complicates the resource allocation procedure. In addition, the inherent properties of mmWave frequencies make a wireless connection more susceptible to blockage. Therefore, this study characterizes resource allocation, interference, and blockage avoidance techniques in the context of IAB networks.

The results of the research demonstrate that interference caused by mutual reception at the IAB node can be avoided using spatial diversity. The critical angular distance of more than 25° is identified as the point at which mutual receptions start to influence each other. The dynamic resource allocation scheme is proposed, which enables load balancing in IAB networks limited by the half-duplex constraint. Finally, multi-connectivity and single connectivity with fast switching are examined as the means to combat the blockage. It is demonstrated that when switching to another gNB, the load should be considered together with the link quality.

Keywords: IAB networks, mmWave frequencies, resource allocation, interference cancellation, multi-connectivity.

Preface

This thesis was written as a part of the project in collaboration between Tampere University and Intel Corporation. Therefore, I would like to thank everyone, who was involved in the work on this project. Especially, I would like to thank my supervisors Assoc. Prof. Sergey Andreev, Dr. Dmitri Moltchanov from Tampere University, and Dr. Hosein Nikopour from Intel Labs for their guidance and help.

Also, I want to thank my family and beloved for supporting me even in the hardest times.

Tampere, 5th August 2021
Yekaterina Sadovaya

Contents

1 Introduction 1
1.1 Current State and Evolution of 5G Systems 1
1.2 Research Questions 2
2 IAB Technology in 3GPP NR 3
2.1 Architecture 3
2.2 Topology Formation and Path Selection 7
2.3 Resource Allocation 9
2.4 Multi-Connectivity and Multi-Beaming 11
3 System Model 15
3.1 Deployment of Interest 15
3.2 Traffic Model 16
3.3 Channel Model 18
3.4 Antenna Model 22
3.5 Blockage Model 25
3.6 UE Mobility Model 28
3.7 Implementation Details 28
4 Numerical Results 33
4.1 Simulator Calibration 33
4.2 Interference Mitigation 35
4.3 Identifying Network Overloaded Regime 38
4.4 Resource Allocation and Multi-Hop Operations 41
4.5 Multi-Connectivity and Multi-Beam Features 44
5 Conclusions 50
References 52

List of Symbols and Abbreviations

3GPP	The 3rd Generation Partnership Project
AMF	Access and Mobility Management Function
AoA	Angle of Arrival
AoD	Angle of Departure
ARQ	Automatic Repeat Request
ASA	AoA Spread in the Azimuth Plane
ASD	AoD Spread in the Azimuth Plane
BAP	Backhaul Adaptation Protocol
BLER	Block Error Rate
CDF	Cumulative Distribution Function
CN	Core Network
CP	Control Plane
CQI	Channel Quality Indicator
CU	Central Unit
DES	Discrete-Event Simulation
DgNB	Donor gNB
DL	Downlink
DS	Delay Spread
FS	Fast Switching
gNB	5G Base Station
IAB	Integrated Access and Backhaul
LoS	Line-of-Sight
LSP	Large-Scale Parameters
MAC	Medium Access Control
MCS	Modulation and Coding Scheme
MIMO	Multiple Input Multiple Output
mmWave	Millimeter-Wave
MPC	Multipath Component
MT	Mobile Termination
NLoS	Non-Line-of-Sight
NR	New Radio
PDCP	Packet Data Convergence Protocol
PDF	Probability Density Function
PDU	Protocol Data Unit
PF	Proportional Fair
PHY	Physical Layers
QoS	Quality of Service

RA	Resource Allocation
RDM	Random Direction Mobility
RLC	Radio Link Control
RPGM	Reference Point Group Mobility
RRC	Radio Resource Control
RSRP	Reference Signal Received Power
Rx	Receiver
SA	Stand-Alone
SDAP	Service Data Adaptation Protocol
SI	Self-Interference
SINR	Signal-to-Interference-plus-Noise Ratio
SMF	Session Management Function
SNR	Signal-to-Noise Ratio
SSP	Small-Scale Parameters
TDMA	Time-Division Multiple Access
TTI	Transmission Time Interval
Tx	Transmitter
UE	User Equipment
UP	User Plane
UL	Uplink
WPF	Weighted PF
ZOA	Zenith angle Of Arrival
ZOD	Zenith angle Of Departure
ZSA	Zenith angle Spread of Arrival
ZSD	Zenith angle Spread of Departure

1 Introduction

1.1 Current State and Evolution of 5G Systems

Nowadays, the next generation of mobile broadband (5G) is becoming a commercial reality. It delivers significantly higher throughput than its predecessors. The promised data rates can reach up to 10 Gbps [10, 8]. This huge improvement in capacity is possible due to the transition to the millimeter-wave (mmWave) spectrum as there is more bandwidth available [36]. Together with advanced signal processing and multi-input and multi-output (MIMO) antennas, mmWave resources offer new capabilities for high data rate and low latency communications [18]. However, radio propagation over mmWave frequencies differs significantly from the propagation in microwave bands. Specifically, it has such inherent properties as higher free-space, reflection, and penetration losses [35]. In addition, mmWave propagation is susceptible to blockage and weather conditions, such as foliage and rainfall [37].

The aforementioned effects limit the coverage area of the new radio (NR) base station (gNB – 5G term for the base station). In addition, the probability of link blockage is increased. Therefore, network operators are forced to deploy ultra-dense cells. However, considering such dense scenarios is costly if all the gNBs are wired [26]. Hence, to lower the deployment cost, 3GPP is considering integrated access and backhaul (IAB) [5], which assumes wireless backhaul and access. This concept is enabled by new entities (IAB nodes), which represent a relay between UEs and the donor gNB (DgNB). Moreover, IAB architecture enables a multi-hop connection, which is not possible with a conventional relay [47]. Several backhaul path selection strategies in the IAB setup are addressed in [32, 44, 41, 48]. Many studies have demonstrated the advantages of IAB in terms of UE data rates [33, 34, 21]. However, this metric is limited by the capacity bottleneck of the wireless backhaul connections [40].

Apart from blockage, ultra-dense scenarios are typically subject to higher interference levels such as inter-cell and self-interference (SI). The avoidance of SI has been studied in [50, 42, 11]. However, these works only address SI due to the full-duplex assumption. Methods to avoid inter-cell interference are evaluated in [27, 23]. The authors of [13] propose an algorithm for signal-to-interference-plus-noise ratio (SINR) improvement assuming mobile IAB nodes. However, SI caused by the simultaneous reception by different antenna sectors of an IAB node has not been addressed so far.

In addition, there are several challenges associated with IAB-specific operations. To enable in-band communications, the resources intended for the backhaul links

should be multiplexed with those provided for the access. However, this forces the system to operate under the half-duplex constraint, which makes the resource allocation (RA) and scheduling procedures challenging. For instance, the regular proportional fair algorithm becomes inefficient due to the asymmetry of IAB networks. While global optimization is solved in [13, 25, 12, 28], it can be computationally inefficient in real-life systems.

In addition to RA and scheduling, other methods exist to enhance the system performance. For example, the authors of [46, 30, 38, 45] demonstrated that multi-connectivity significantly increases per-user throughput due to the fact that the load in the network is distributed evenly. An analytical model for multi-connectivity in 5G mmWave urban deployments was also developed in [16]. Furthermore, the switching strategies are discussed in [31, 43] while a handover probability analysis was conducted in [49]. Moreover, multiple switching techniques can be considered as an efficient means to combat the link blockage effect. However, multi-connectivity in the listed works is only addressed without a reference to the IAB concept. Moreover, IAB architecture allows incorporating such options as multi-beaming and multi-hopping. On the other hand, their impact on the throughput remains unclear.

1.2 Research Questions

In summarizing the literature review, this thesis aims to fill the gaps in the IAB-related studies. The main goals of the thesis are the following:

- Assess inter-sector interference in an in-band IAB network.
- Estimate the impact of angular and spatial diversities as interference mitigation methods and determine the target level of angular and spatial diversities suitable for given deployment restrictions.
- Quantify the effects of advanced functionalities in IAB networks. These functionalities include multi-hopping, multi-beaming, and multi-connectivity operations.
- Evaluate the impact of dynamic RA schemes and compare the throughput with the static resource allocation.

Following this introduction, the thesis is organized as follows. Chapter 2 starts with a description of the IAB technology and its standardization phases. This is followed by Chapter 3, which gives a detailed insight into the developed system model. This chapter explains the methodology used in this work and also gives the definitions of the models included in the simulations. The numerical results from the conducted studies are reported and analyzed in Chapter 4 and the main conclusions are presented in Chapter 5.

2 IAB Technology in 3GPP NR

This chapter includes a summary of the IAB technology specified by 3GPP. First, the architecture of IAB systems with the involved interfaces and protocols is described. Then, topology management is discussed, i.e. route selection in case of multi-hop operation. Finally, RA and optimization-related aspects are addressed.

2.1 Architecture

There are two ways of implementing the wireless backhaul, i.e. in-band and out-of-band backhaul. In the case of in-band backhauling, access and backhaul links operate within the same frequency band that causes the half-duplex constraint. Specifically, this constraint means that an IAB node cannot transmit and receive at a time. On the one hand, out-of-band scenarios are not subject to the half-duplex constraint. On the other hand, it is crucial to study in-band backhauling, which offers a simpler handover procedure and tighter interconnection between access and backhaul. However, architectures, which are discussed below are applicable for in-band and out-of-band backhauling solutions.

3GPP defines architecture of IAB nodes in [5]. The IAB technology specification presumes the reuse of existing access-oriented interfaces and functions at the backhaul links. These functions contain access and mobility management function (AMF), mobile-termination (MT), session management function (SMF), and user plane (UP) function. In IAB networks, the MT function terminates the Uu interface at the backhaul, which is responsible for the connection between IAB nodes or the DgNB. The UPF is responsible for the quality of service (QoS) as well as for the UP data. The involved interfaces include F1, NR Uu, X2, N4, and NG. The AMF holds functions of the control plane (CP), i.e., authentication control, mobility management, and security. The protocol data unit (PDU) sessions are handled by the SMF. As an example, IAB architecture with the utilized interfaces is provided in Fig. 2.1. In this example, the network operates in stand-alone (SA) mode. In non-SA mode, the IAB node employs the NR link only for the backhaul. In addition, the DgNB may consist of a central unit (CU) and a distributed unit (DU) or it may consist only of a CU.

3GPP describes two architecture groups in TR 38.874 [5]. The first one assumes the CU/DU split while several configurations in the second group propose the non-split architectures of the DgNB. The architecture, which is given in Fig. 2.2 corresponds to architecture 1a. The CP and UP protocol stacks for a multi-hop IAB network are depicted in Fig. 2.2. IAB architecture introduces a new protocol for the

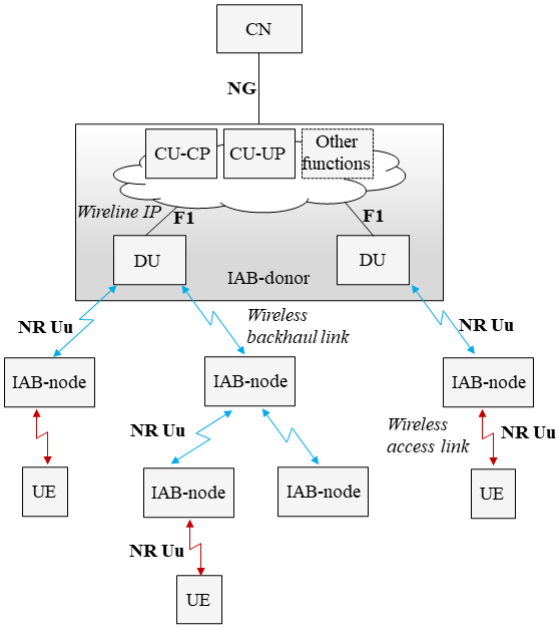

Figure 2.1 *Example of IAB architectures in SA mode [5].*

UP to support multi-hop backhauling, which is named backhaul adaptation protocol (BAP). The application protocol F1-AP is employed on the CP for transferring lower layer configuration information between the CU and DU.

The connection to the core network (CN) is established by a CU via the NG interface. It is responsible for service data adaptation protocol (SDAP), radio resource control (RRC), and packet data convergence protocol (PDCP). A DU is responsible for radio link control (RLC), medium access control (MAC), and physical (PHY) layer functions. The DU is connected to the CU via the F1 interface. The CU/DU split is motivated by the following fact. The delay-critical applications, for example, MAC scheduling, are realized in the DU. On the other hand, less critical operations are handled by the CU. Therefore, the split architecture is more convenient for multi-hop backhaul.

In architecture 1a, it is assumed that an IAB node is served by only one DgNB. Architecture 1b is offered in Fig. 2.3(a). In this architecture, an IAB node can have more than one connection with an upstream IAB node or the DgNB. In addition, IAB nodes can consist of multiple DUs, where each DU is connected to the CU of the DgNB via F1-C interface. Furthermore, in contrast to architecture 1a, the MT of an IAB node set up a PDU session via a UPF on the DgNB side. Further, the PDU session carries F1* interface for the DU. Therefore, the PDU session enables a point-to-point connection between the CU and DU.

In architectures 1a and 1b, an adaptation layer is integrated with MAC or placed above the MAC layer. The adaptation layer can be separated from the other layers or it may comprise several sublayers. For example, GTP-U header or IP header can

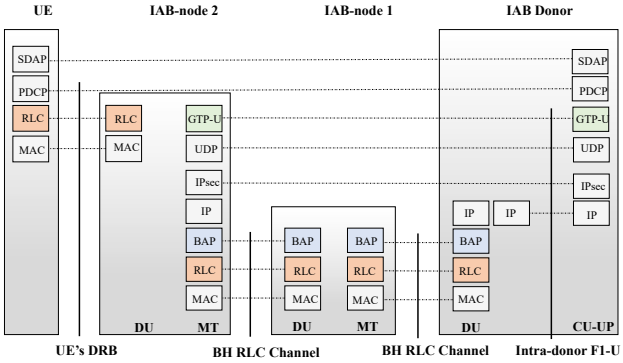

(a) UP protocol stack.

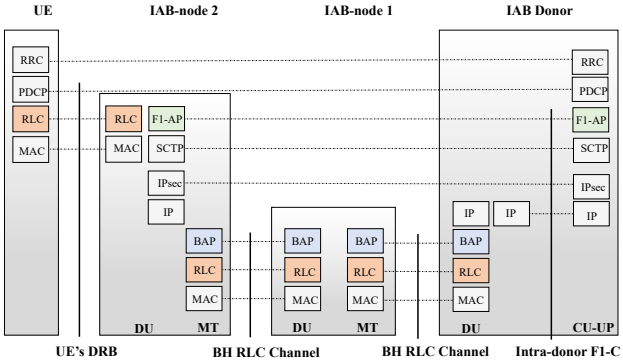

(b) CP protocol stack.

Figure 2.2 *CP and UP protocol stacks for IAB networks for architecture 1a.*

be a part of the adaptation layer. Depending on the architecture, the adaptation layer is responsible for different functions. For architecture 1a, these functions are:

- UE bearer identification;
- Providing QoS by the scheduler in the downlink (DL) and in the uplink (UL) over the wireless backhaul;
- Mapping PDUs of the UEs to the backhaul RLC channels;
- Routing according to the topology of the wireless backhaul network.

For architecture 1b, the adaptation layer is responsible for the following functions:

- Routing according to the topology of the wireless backhaul network.
- Mapping PDUs of the UEs to the backhaul RLC channels;
- Providing QoS by the scheduler in the DL and in the UL over the wireless backhaul.

The second group of IAB architectures offers 3 different architectures, i.e., 2a, 2b, and 2c. The reference diagram for architecture 2a is given in Fig. 2.3(b). Note that

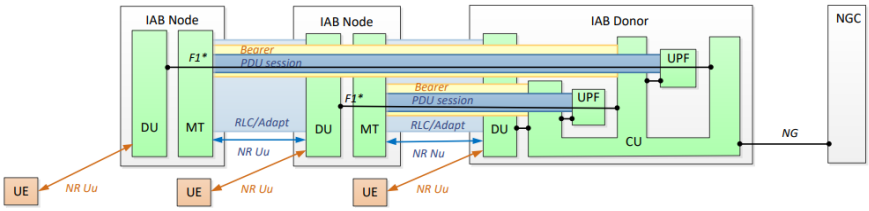

(a) IAB architecture 1b.

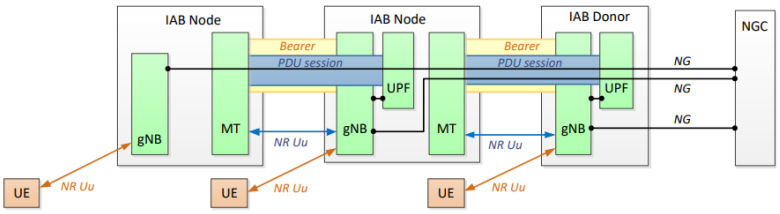

(b) IAB architecture 2a.

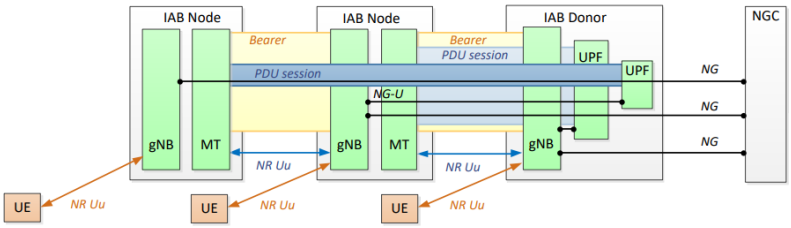

(c) IAB architecture 2b.

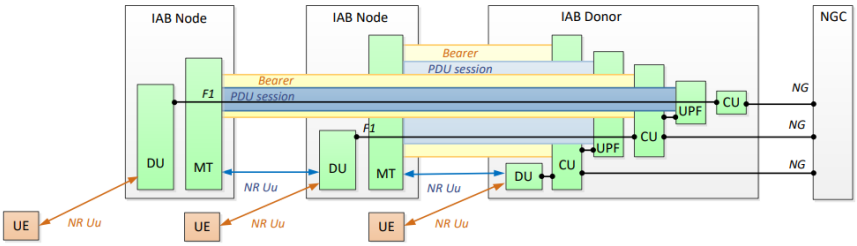

(d) IAB architecture 2c.

Figure 2.3 *Reference diagrams for IAB architectures 1b, 2a, 2b, and 2c.*

architectures 2a and 2b do not leverage the CU/DU split. In this architecture, the NR Uu link serves to support a PDU session with the UPF. Therefore, PDU sessions on backhaul links are generated independently. Then, an IAB node forwards the data between the neighboring links. In this setup, an IAB node can be connected to multiple IAB nodes or DgNBs. The diagram for architecture 2b is depicted in Fig. 2.3(c). Similar to architecture 2a, the MT establishes a PDU session with the UPF. However, the UPF is located at the DgNB in this architecture. In both architectures, 2a and 2b, the IP-based interfaces such as F1, NG, Xn, and N4 are carried over IP plane forwarding in the wireline backhaul network.

In contrast to previous architectures of the second group, architecture 2c leverages the CU/DU split. In addition, each IAB node has an MT function, which is responsible for the establishment of an RLC channel with the DU of the parent IAB node or the DgNB. The DgNB comprises DU, CU, and UPF functions. It is worth noting that a CU and a UPF are created for each of the connected IAB nodes. A PDU session is established by the MT of an IAB node with the UPF of the DgNB. As in architectures 2a and 2b, IP-connectivity to the wireline backhaul network is supported.

According to 3GPP specifications, IAB architectures support hop-by-hop and end-to-end RLC automatic repeat request (ARQ). Depending on the ARQ implementation, different interdependencies between RLC ARQ and the adaptation layer are assumed. Specifically, for end-to-end ARQ, the adaptation layer is integrated with MAC or located above the MAC layer. In the case of hop-by-hop ARQ, there is no interdependence between RLC ARQ and the adaptation layer. The choice of the ARQ implementation depends on the network requirements. For instance, hop-by-hop ARQ may provide higher delay as packets should pass through all the RLC states on every hop. However, this is not relevant for a network with poor channel conditions as the lost packets have to be retransmitted on multiple links.

2.2 Topology Formation and Path Selection

IAB nodes enable multi-hop backhauling, which allows for flexible coverage extension in 5G NR deployments. In multi-hop systems, the network performance heavily depends on the number of hops between UEs and a service node. Therefore, topology formation and path selection are crucial for IAB networks. As it was mentioned, IAB nodes hold two functions, i.e., DU and MT. The DU is responsible for the connection with UE or a child IAB node. The MT function is required to support the connection with a parent. The data radio bearers (DRBs) are multiplexed by an IAB node into the backhaul RLC channels, which are utilized to transport packets between the DgNB and IAB nodes.

An IAB network is established via the following steps. Initially, a parent of an IAB node is selected by the MT. Further, an RRC connection with the CU is set up. The backhaul link is initialized using the RLC connection. At this stage, a new routing protocol named BAP is introduced, which is responsible for the packet forwarding over the multi-hop backhaul topology. Then, the IAB node sets up the DU function, which corresponds to the opening of the F1-C connection. After the topology is configured, it is adapted further based on the load and environmental conditions. During this procedure, information about the load of the IAB nodes and the link quality is broadcasted by the MT of an IAB node to the CU, which allows efficient resource allocation at the CU.

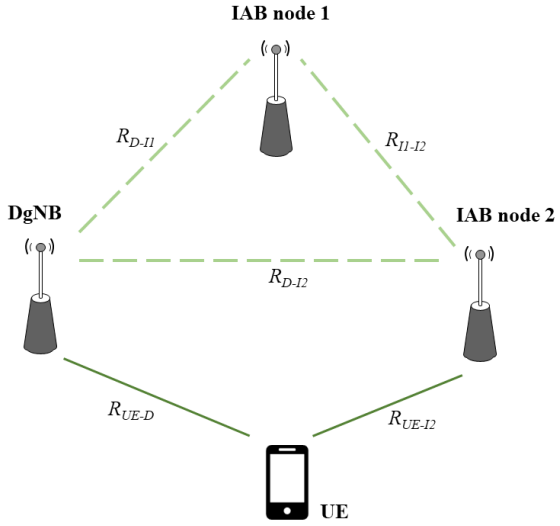

Figure 2.4 *Example of path selection options in an IAB network.*

There are several 3GPP contributions where topology formation strategies are discussed [1, 6]. The impact of the number of activated IAB nodes is studied in [1], where it is demonstrated that the overall network performance depends on the chosen IAB node activation sequence. This aspect is essential from the practical implementation point of view as the reference signal received power (RSRP) measurements from the IAB nodes are not available to the network when the activation decision is made. Therefore, optimal topologies based on the maximum RSRP are not always possible in real-life IAB systems. The performance of IAB networks with different topologies is evaluated in [6], where it is concluded that accounting for load conditions is crucial at the topology establishment phase.

In this work, two path selection strategies are considered. The first one is based on the maximum RSRP criterion, which assumes the maximum of RSRP minima. As an example, the network deployment in Fig. 2.4 is considered. In this scenario, the UE can reach the DgNB and the IAB node 2. The connection between the UE and the DgNB is denoted as R_{UE-D} while the connection between the UE and the IAB node 2 is denoted as R_{UE-I2}. On the other hand, both the DgNB and the IAB node 2 can reach IAB node 1. Therefore, the possible paths for the UE to communicate with the DgNB are R_{UE-D}, R_{UE-I2}-R_{D-I2}, and R_{UE-I2}-R_{I1-I2}-R_{D-I1}. According to the maximum RSRP strategy, the path will be selected as

$$\max(R_{UE-D}, \min(R_{UE-I2}, R_{D-I2}), \min(R_{UE-I2}, R_{I1-I2}, R_{D-I1})). \tag{2.1}$$

The second strategy is based on the minimum number of hops criterion. In this strategy, UEs perform measurements with IAB nodes only if the DgNB becomes unavailable. This can happen due to mobility or link blockage. Otherwise, the UE

always attempts to connect to the DgNB. The potential benefit of the path selection based on the minimum number of hops is a lower delay as the average number of hops in the network tends to one.

2.3 Resource Allocation

The traffic from access and the backhaul links must be multiplexed to provide the support of in-band operations. However, in this case, an IAB node is subject to the half-duplex constraint. This is required to guarantee a feasible handover procedure. As it is recommended by 3GPP, resources should be partitioned via the time-division multiple access (TDMA) [5]. On the other hand, simultaneous transmission and reception at IAB nodes can be enabled using multiple antenna sectors. In addition, several multi-beam deployments are applicable for IAB networks, especially mmWave. However, additional beams decrease the transmit power due to the fact that the power is split among the beams. Hence, if it is assumed that the slot is divided into two parts, the following transmissions are allowed in the first one: from DgNB to IAB node; from DgNB to UE; from UE to IAB node. Similarly, the opposite transmissions happen in the second part of the slot.

Three different methods for RA design can be considered, which are illustrated in Fig. 2.5. The first one is a baseline, where the same amount of resources is allocated for UL and DL transmissions. In this case, the slot division coefficient between UL and DL is 0.5. While this division enables a straightforward implementation, it does not account for situations where one of the logical directions is more loaded. On the other hand, the half-duplex constraint establishes asymmetry in IAB networks. For instance, in Fig. 2.5, UL transmissions are in the first part of the slot of an IAB node while the DgNB transmits in DL at this time. To avoid conflicts induced by the half-duplex constraint, the border of two slots should be synchronized.

To implement proportional fair (PF) RA in the considered network, the number of active UEs in UL and DL should be reported by the CU. UE is considered active if there is buffered traffic in one of the logical directions. Once this information is provided, the slot division coefficient in the DL is calculated as

$$C_{DL} = N_{DL}/N_{tot}, \tag{2.2}$$

where N_{DL} is the number of active UEs in the DL direction; N_{tot} is the total number of active UEs in the UL and DL. Similarly, the slot division coefficient in the UL can be calculated as

$$C_{UL} = N_{UL}/N_{tot}, \tag{2.3}$$

where N_{UL} is the number of active UEs in the UL N_{UL} direction. Then, the resources are allocated equally among UEs in the UL or DL.

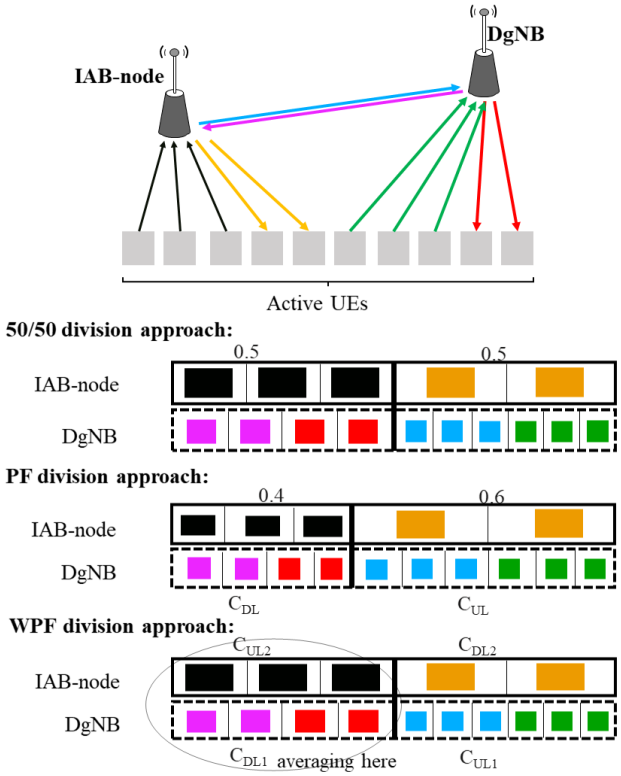

Figure 2.5 *Considered RA schemes.*

The third approach is called weighted PF (WPF) and it aims to add more fairness into PF RA by the additional weighting of the coefficients. In addition to the number of active UEs, it requires additional information regarding the traffic. Specifically, it should be known by the scheduler to/from which node the traffic is transferred. Once this information is provided, the separate coefficients for the DgNB and IAB nodes can be computed. For example, in Fig. 2.5, the coefficient C_{DL1} is calculated as

$$C_{DL1} = N_{DL_{DgNB}}/N_{tot_{DgNB}}, \tag{2.4}$$

where $N_{DL_{DgNB}}$ is the number of active UEs in the DL, which are connected to the DgNB; $N_{tot_{DgNB}}$ is the total number of active UEs connected to the DgNB. The C_{UL2} is computed for the IAB node in a similar manner:

$$C_{CU2} = N_{UL_{IAB}}/N_{tot_{IAB}}, \tag{2.5}$$

where $N_{UL_{IAB}}$ is the number of active UEs in the DL, which are connected to the IAB node; $N_{tot_{IAB}}$ is the total number of active UEs connected to the IAB node. Then, the final coefficient can be obtained as the average between the parallel coefficients. For example in Fig. 2.5, $C_{DL} = (C_{DL1} + C_{CU2})/2$. The advantage of this averaging procedure is improved fairness. Specifically, it might be beneficial for asymmetric scenarios, e.g., when the number of active UEs in the DL connected to the IAB node is much smaller than the number of active UEs in the UL connected to the DgNB.

2.4 Multi-Connectivity and Multi-Beaming

One of the major challenges in mmWave networks is robustness since mmWave signals can be blocked by typical objects in an environment such as human bodies. Multi-connectivity allows enhancing the reliability of a network. This improvement is achieved due to the simultaneous support of several links. It is worth noting that to achieve the gain by using multi-connectivity schemes, the links should be spatially uncorrelated. The maximum number of simultaneously supported links is dictated by the system. This number is called the degree of multi-connectivity. Multi-connectivity is ratified in 3GPP Rel. 15 TS 37.340 [2]. According to the specifications, multi-connectivity is possible among mmWave cells and 4G cells. In this work, by multi-connectivity, it is assumed that UE may preserve simultaneous connections with several IAB nodes or DgNBs.

Although multi-connectivity has not been considered in the context of IAB networks so far, it can bring advantages due to the following reasons. The additional backup link allows for decreasing blockage rates. There are different ways to implement multi-connectivity. For example, both channels can be employed at the same time or one connection can serve as a backup link. However, in the case of in-band backhaul implementation, scheduling poses a problem due to the half-duplex constraint. Specifically, two types of conflicts are possible in the considered IAB setup. They are depicted in Fig. 2.6. Fig. 2.6(a) represents a situation where no conflicts occur in the network. However, if the number of active users connected to the IAB node 2 in the UL and DL changes, conflicts may arise. This situation is reflected in Fig. 2.6(b) where it is assumed that UEs corresponding to the IAB node 2 in the UL direction was served. It can be seen that total transmission time, in this case, is larger than 50 % of the slot. To avoid this conflict in the simulations, it is required to check that the total transmission time is not more than 50 % and reduce it. The second type of conflict represents the violation of the half-duplex. This may happen in the case that UE establishes multi-connectivity with an IAB node and the DgNB due to the asymmetry in slots. For example, in Fig. 2.6(c) UE, which utilizes multi-connectivity functionality cannot transmit and receive at a time. This conflict can be bypassed via permutations in schedules. Therefore, the task of a scheduler is to determine possible intersections of receive/transmit intervals among the UEs, which allows preventing violation of the half-duplex constraint.

Another challenge, which is faced, while deploying an IAB network with the support of multi-connectivity is the joint implementation of multi-connectivity and multi-hopping. Two different topologies with and without multi-connectivity are illustrated in Fig. 2.7 where D stands for the DgNb and I stands for the IAB node. When multi-connectivity is disabled in a multi-hop network, the topology of

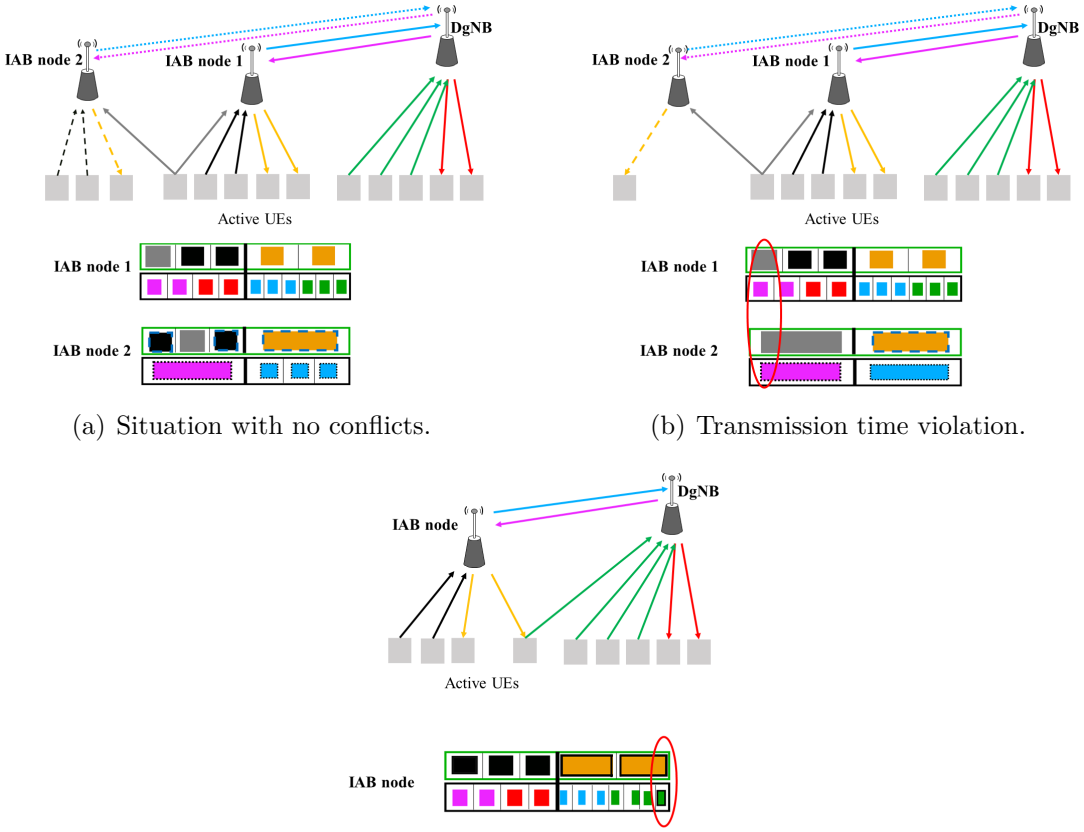

(a) Situation with no conflicts.

(b) Transmission time violation.

(c) Half-duplex constraint violation.

Figure 2.6 *Types of conflict situations, which may occur in an in-band IAB network with multi-connectivity operation.*

this network corresponds to a tree topology (see Fig. 2.7(a)). According to a tree topology, only one link exists between two connected nodes. Therefore, the half-duplex constraint is not violated. A completely different situation is observed when multi-connectivity is enabled in a multi-hop network. Due to the fact that with multi-connectivity each node may have multiple connections, the topology forms a directed acyclic graph. In this case, a child can have several parents. This situation is depicted in Fig. 2.7(b) where the second connections are enumerated as 1 and 2. As can be seen from the example, connection 1 is forbidden as it violates the half-duplex constraint. On the other hand, connection 2 is supported because it does not violate the half-duplex constraint. Accordingly, only transmissions from even levels to odd levels are allowed in the considered topology. It can be implemented in the simulations by dividing the transmissions via TDMA.

Moreover, several advanced functionalities can be incorporated together with the multi-connectivity operation such as fast switching (FS) and regular scanning. FS means that the association point can be changed if the current one becomes

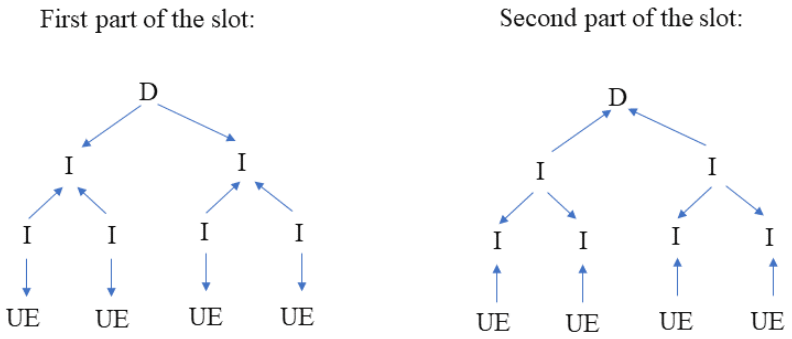

(a) Multi-hop topology with single connectivity.

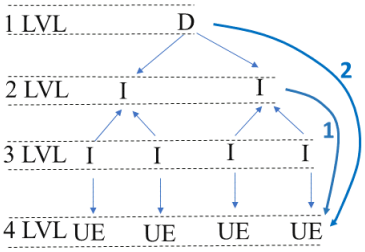

(b) Multi-hop topology with multi-connectivity.

Figure 2.7 *Topologies with and without multi-connectivity function.*

blocked/unavailable. Further, when UE is switched to another association point, it s assumed that no re-switching occurs. The re-switch will be done only in case that the newly established association point becomes unavailable. In this work, the switching point is chosen based on the highest RSRP level. This implementation of FS can be improved by the incorporation of the re-switching capabilities. In the improved version, when the association point was changed, UE may still restore the previous connection if the following two criteria are satisfied:

- It is not blocked.
- The RSRP value is higher than the RSRP value on the current link.

In addition, regular scanning can be performed, which implies a continuous update of the RSRP measurements from IAB nodes and DgNBs. Further in this thesis, the improved variant of FS is referred to as FS improved by regular scanning. It is worth noting that these advanced capabilities are crucial for systems, which are affected by such dynamic factors as link blockage and mobility.

In IAB systems, multi-beam functionality can be employed at both DgNB and IAB nodes. Multi-beam communication involves several independent directional beams generated from a single aperture, which can be utilized simultaneously. This is a hardware solution, which is based on phased antenna arrays. On the one hand,

this functionality enables significant capacity boost and provides frequency reuse, which results in a higher number of subscribers. On the other hand, the transmit power is split between the [20] beams; thus, it is reduced accordingly. Another challenge for multi-beam transmission is associated with that the beams might not be limited by the desired coverage areas due to sidelobe intersections and finite-gain roll-off. The latter can be overcome by increasing the antenna size and its complexity. However, this results in a higher cost of equipment. More details regarding beam management strategies can be found in [24, 29, 22].

In this thesis, different multi-beam options are considered. The main goal is to quantify their impact on the UE throughput. These options are:

- All multi-beam.
- DgNB is multi-beam.
- All single beam.

In all multi-beam deployment, IAB nodes and DgNBs utilize multi-beam functionality, i.e., IAB nodes and DgNBs have separate beams for each backhaul connection and access beams for UEs. Moreover, the transmit power is split according to the number of beams. The second considered case corresponds to a situation when only the DgNB has multi-beam capabilities. In this scenario, the DgNB only has separate beams for the backhaul connections. Therefore, the transmit power according to the number of IAB nodes. It is practical to consider this setup since it provides a trade-off between increasing the resources and reducing the coverage. The last case, which was assessed, is all single beam deployment where IAB nodes and DgNBs employ a single beam setup.

3 System Model

In this chapter, the main parts of the simulation tool are discussed in detail. The chapter starts with a description of the scenario. Then, proceeds to the main modeling abstractions, i.e. channel, antenna, blockage, and UE mobility models. The last section covers additional implementation aspects such as interference reduction methods and software-related features.

3.1 Deployment of Interest

The modeling scenario and the choice of parameters are based on the effective 3GPP recommendations for evaluating the IAB systems as defined in TR 38.874. The scenario is illustrated in Fig. 3.1. The parameters utilized for the numerical assessment are given in Table 3.1.

Table 3.1 *Parameters utilized for numerical assessments.*

Parameter	**Value**
Carrier frequency	30 GHz
Bandwidth	400 MHz
Number of UEs	30, 60
Cell radius	500m
Tx power of DgNB	40 dBm
Tx power of IAB	33 dBm
Tx power of UE	23 dBm
Noise figure of DgNB and IAB	7 dB
Noise figure of UE	13 dB
Power spectral density of noise	-173.93 dBm/Hz
Interference margin	3 dB
Antenna array of UE	4x4
Antenna array of DgNB and IAB	16x16
Velocity of UE	3 km/h
Height of a blocker	1.7 m
Radius of a blocker	0.1 m
Height of DgNB	25 m
Height of IAB	10 m
Height of UE	1.5 m

Two different configurations were utilized for SI assessment and characterization of advanced functionalities. In the SI-related study, a single IAB node is considered. An isolated IAB node is sufficient due to the fact that the main aim is to characterize SI and investigate SI mitigation techniques. The IAB node is placed in the center.

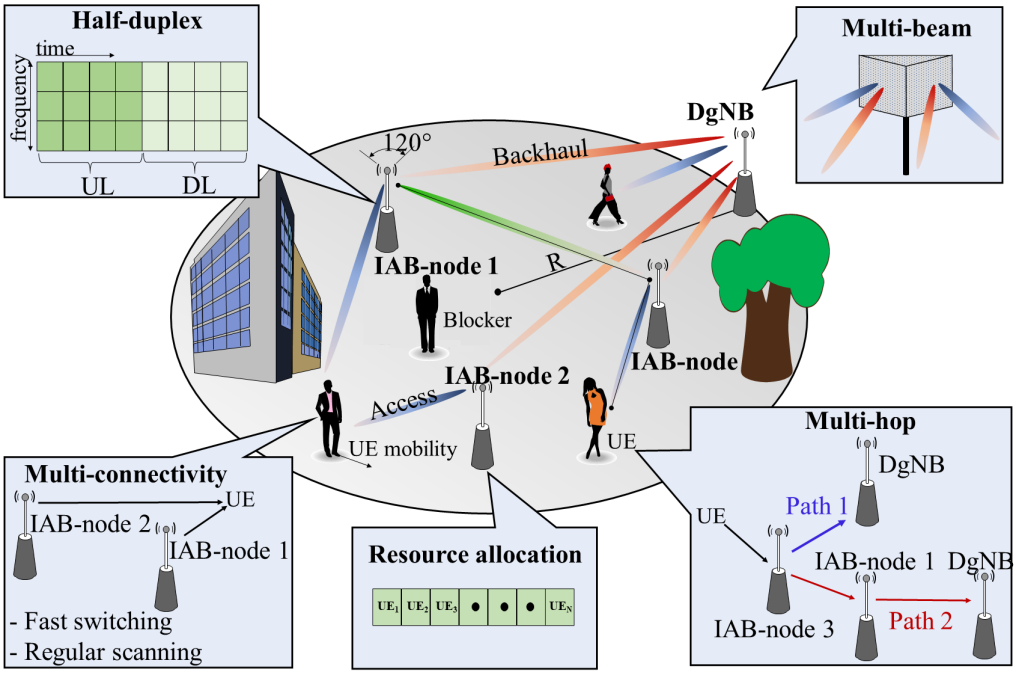

Figure 3.1 *Considered 3GPP IAB deployment.*

The DgNB is located at the edge of the cell with one of its sectoral antennas pointing at the cell. Therefore, the distance between the DgNB and the IAB node equals R. It is worth noting that R is selected in a way that no UEs experience an outage within this radius. It is worth noting that multi-connectivity and multi-beam capabilities are disabled. In addition, full-buffer traffic is assumed.

For evaluation of the throughput benefits from using advanced functionalities, the number of IAB nodes is not limited to one. Similar to the previous scenario, the DgNB is placed at the cell edge while the UEs and IAB nodes are deployed randomly. In addition, dynamic traffic is assumed. The rest of the assumptions are common for both studies. The sectorized antenna is utilized at the IAB node. Those UEs, which are served by the same antenna sector are multiplexed via TDMA. In addition, UE mobility is included in the simulations. Moreover, the half-duplex constraint is accounted for, which states that the IAB node can either transmit or receive at a time.

3.2 Traffic Model

Following the 3GPP recommendations, the traffic of each UE in the UL and DL is assumed to follow FTP model 3 (see Fig. 3.2). It is based on FTP model 2, which is defined by the 3GPP in TR 36.814. Accordingly, data arrivals are separated by an exponential idle time with the parameter λ, which defines the session arrival rate,

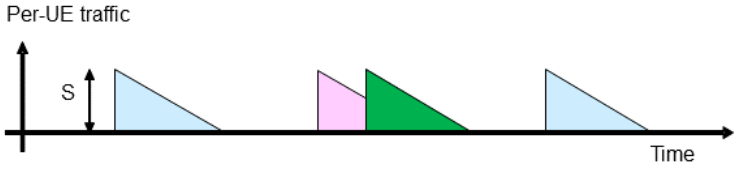

Figure 3.2 *Illustration of the employed traffic model.*

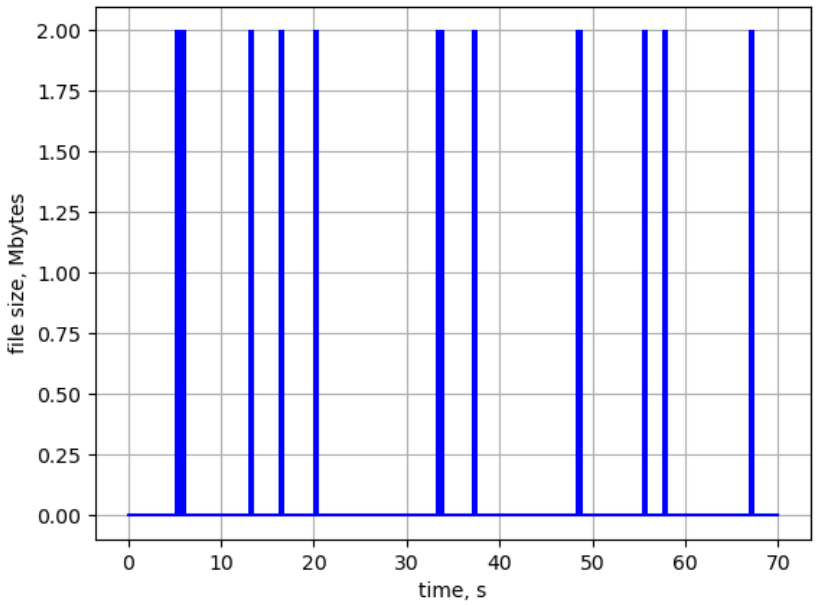

Figure 3.3 *Simulated traffic with $\lambda = 0.2$ sessions/second.*

thus forming a Poisson arrival process:

$$P(A_n \leq t) = 1 - exp(-\lambda t). \tag{3.1}$$

Fig. 3.3 demonstrates an example of traffic generation taken from the simulation framework with session arrival rate of 0.2 sessions/second. This distribution holds a specific mean and variance equal λ. In this model, the file size $S = 2$ Mbytes is employed. The number of UEs is fixed while the traffic at each UE is independent of others. It is worth noting that models, which are based on a Poisson distribution are the most widely used in network analysis. This is because Poisson processes demonstrate a number of various mathematical properties, which reflect real-life traffic patterns. First, the superposition of independent Poisson processes leads to a new Poisson process. Moreover, the rate of the new process equals the sum of the rates of independent Poisson processes. Second, the independent increment property makes the Poisson process memoryless. Therefore, the Poisson process is typical for traffic simulations.

3.3 Channel Model

In this thesis, the 3GPP cluster channel model [4] is adopted for channel modeling. The procedure of channel generation can be also described via the steps, which are depicted in Fig. 3.4. The first step involves the setup of network parameters such as the number of UEs and gNBs, their locations, scenario type, antenna patterns, and center frequency. Then, the propagation conditions are specified. In this work, the propagation conditions are determined based on the blockage probability, which is generated separately for each link. When the propagation conditions are known, the PL can be calculated using (3.2), which is given for each DgNB-UE or IAB-UE link as

$$L_{UMa-LoS} = \begin{cases} L_1, & 10 \text{ m} \leq d_{2D} \leq d_{BP} \\ L_2, & d_{BP} \leq d_{2D} \leq 5 \text{ km}, \end{cases} \tag{3.2}$$

where the branches are given by

$$\begin{aligned} L_1 &= 28 + 22\log_{10}(d_{3D}) + 20log_{10}(f_c), \\ L_2 &= 28 + 40\log_{10}(d_{3D}) + 20\log_{10}(f_c) - \\ &\quad - 9(\log_{10}(d_{BP})^2 - (h_{BS} - h_{UE})^2), \end{aligned} \tag{3.3}$$

while d_{2D} and d_{3D} are the 2D and 3D distances between UE and DgNB/IAB node, f_c is the carrier frequency in MHz, and d_{BP} is the breakpoint distance, which is given as

$$d_{BP} = 4\frac{h_{BS}h_{UE}f_c}{c}, \tag{3.4}$$

where h_{BS} is the height of DgNB h_{DgNB} or IAB node h_{IAB} in m; c is the speed of light.

At the next step, other large-scale parameters (LSPs) are obtained. The LSPs contain the delay spread (DS), AoD and AoA spreads in azimuth and zenith planes, Ricean K-factor [4], and shadow fading (SF). The relation between the LSPs is further described with the correlation coefficient matrix, which is calculated using the Cholesky decomposition. In 3GPP TR 38.901 [4], these coefficients are provided in Table 7.5-6. It is worth noting that the LSPs are uncorrelated between different IAB-UE and DgNB-UE links. The LSPs and small-scale parameters (SSPs) in the simulations follow the UMa line-of-sight (LoS) deployment.

The SSPs are generated first to create MP components (MPCs) with specific parameters. The cluster delays n are generated randomly using the distribution, which is defined for the delay in [4]. Therefore, the delay of the n-th cluster can be written as

$$\tau_n = -r_\tau \text{DSln}(X_n), \tag{3.5}$$

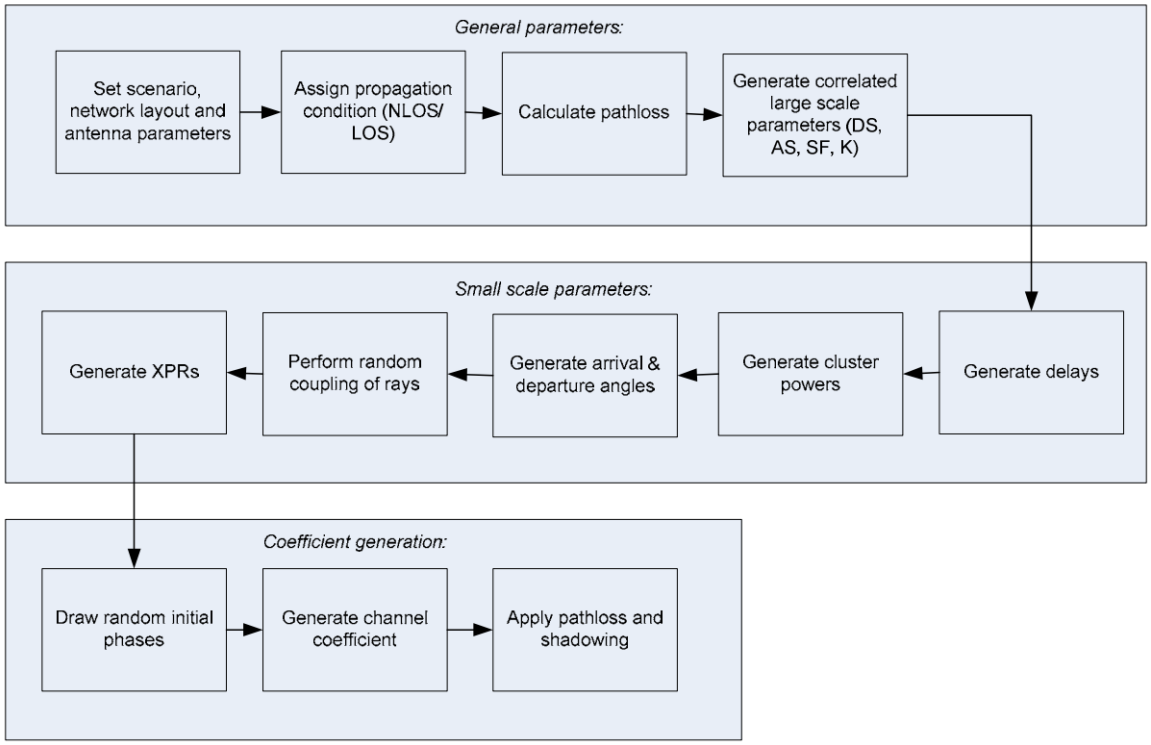

Figure 3.4 *Channel coefficients generation procedure [4].*

where $X_n \sim U(0,1)$ and r_t is the delay distribution proportionality factor. Similarly, the power angular spectrum is obtained using a wrapped Gaussian variable. Hence, the n-th cluster power corresponds to

$$P_n = \exp\left(-\tau \frac{r_\tau - 1}{r_\tau \mathrm{DS}}\right) 10^{-\frac{Z_n}{10}}, \tag{3.6}$$

where Z_n is the SF per cluster in dB. Further, this power needs to be normalized so that the sum of all powers of all the MPCs is equal to one:

$$P_n = \frac{P_n^{'}}{\sum_{n=1}^{N} P_n^{'}}. \tag{3.7}$$

It is worth noting that if the propagation condition corresponds to the LoS case, the LoS component is added to the first cluster, which has the power of

$$P_{1,LoS} = \frac{K_R}{K_R + 1}, \tag{3.8}$$

where K_R is the Ricean K-factor. Therefore, the normalized power yields

$$P_n = \frac{1}{K_R + 1} \frac{P_n^{'}}{\sum_{n=1}^{N} P_n^{'}} + \delta(n-1) P_{1,LoS}, \tag{3.9}$$

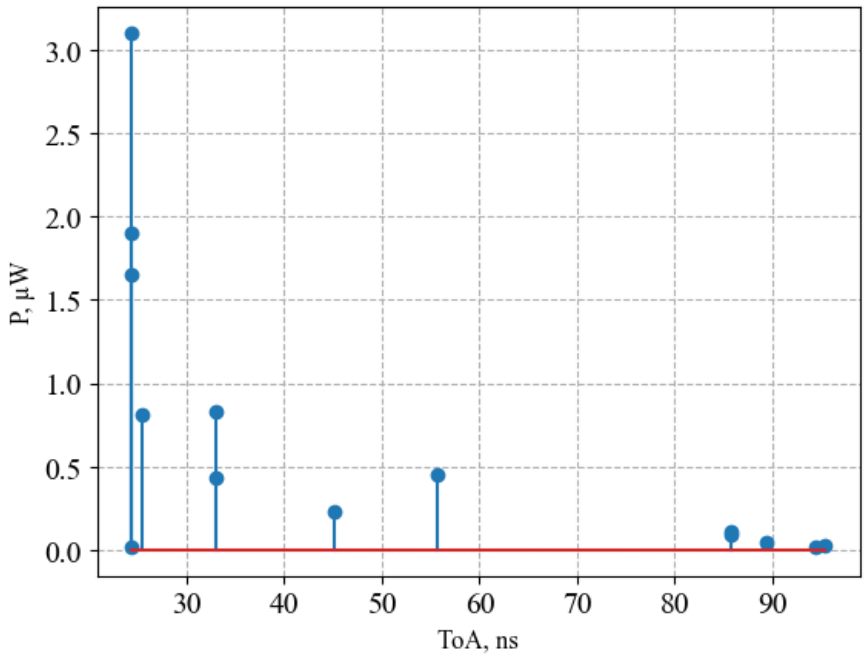

Figure 3.5 *Example of the simulated CIR.*

where δ is the Dirac's delta function.

After the power values for each MPC cluster were determined, the angles of arrival and departure are generated in both azimuth and elevation planes. For instance, AoAs are determined using the inverse Gaussian function as

$$\phi'_{AoA_n} = \frac{2(\mathrm{ASA}/1.4)\sqrt{-\ln(P_n/\max(P_n))},}{C_\phi}, \tag{3.10}$$

where ASA is the AoA spread in the azimuth plane. In (3.10), the value of C_ϕ is defined as

$$C_\phi = \begin{cases} C_\phi^{NLoS}(1.1035 - 0.028K_R - 0.002K_R^2 + 0.0001K_R^3), \text{for LoS} \\ C_\phi^{NLoS}, \text{for NLoS}, \end{cases} \tag{3.11}$$

where C_ϕ^{NLoS} is the scaling factor, which depends on the total number of clusters and is given in [4]. For instance, if the number of clusters is 10, $C_\phi^{NLoS} = 1.09$. For the LoS case, C_ϕ^{NLoS} depends also on the value of K-factor K_R and requires additional scaling to compensate the impact of the addition of LoS peak into the angular spread. Moreover, ϕ_{AoA_n} should be multiplied with the random variable X_n, which can be 1 or -1. This is needed to introduce random variations. Hence, ϕ_{AoA_n} is expressed as

$$\phi_{AoA_n} = X_n\phi'_{AoA_n} + Y_n + \phi_{LoS,AoA}, \tag{3.12}$$

where Y_n $N(0, (\mathrm{ASA}/7)^2)$; $\phi_{LoS,AoA}$ is the direction of LoS, which is defined at the

first step. For the LoS case,

$$\phi_{AoA_n} = (X_n \phi'_{AoA_n} + Y_n) - (X_1 \phi'_{1,AoA} + Y_1 - \phi_{LoS,AoA}). \tag{3.13}$$

The offset angles are added to (3.12) and (3.13). A similar procedure is performed to generate ZOA and ZOD.

Then, the rays within a cluster are coupled together randomly. Further, a cross-polarization power ratio (XPR) κ is generated for each MPC in a cluster. It is determined for each m-th ray of n-th cluster as

$$\kappa_{n,m} = 10^{X_{n,m}/10}, \tag{3.14}$$

where $X_{n,m} \sim \mathcal{N}(\mu_{XPR}, \sigma^2_{XPR})$. As can be seen from (3.14), XPR follows log-Normal distribution.

The final channel coefficients are calculated from the LSPs and SSPs. Before this procedure, the initial phases for each MPC within a cluster are drawn from the uniform distribution within $(-\pi, \pi)$ for different polarization combinations. The final channel coefficient between transmitter (Tx)-receiver (Rx) pair for m-th ray of n-th cluster can be expressed as

$$H^{NLoS}_{Tx,Rx,n}(t) = \sqrt{\frac{P_n}{M}} \sum_{m=1}^{M} \begin{bmatrix} F_{rx,\theta}(\theta_{n,m,ZOA}, \phi_{n,m,AOA}) \\ F_{rx,\phi}(\theta_{n,m,ZOA}, \phi_{n,m,AOA}) \end{bmatrix}^T \begin{bmatrix} e^{j\Phi^{\theta\theta}_{n,m}} & \sqrt{\kappa^{-1}_{n,m}} e^{j\Phi^{\theta\phi}_{n,m}} \\ \sqrt{\kappa^{-1}_{n,m}} e^{j\Phi^{\phi\theta}_{n,m}} & e^{j\Phi^{\phi\phi}_{n,m}} \end{bmatrix} \tag{3.15}$$

$$\begin{bmatrix} F_{tx,\theta}(\theta_{n,m,ZOD}, \phi_{n,m,AOD}) \\ F_{tx,\phi}(\theta_{n,m,ZOD}, \phi_{n,m,AOD}) \end{bmatrix} e^{\frac{j2\pi \hat{r}^T_{rx,n,m)} \bar{d}_{rx,tx}}{\lambda_0}} e^{\frac{j2\pi \hat{r}^T_{tx,n,m)} \bar{d}_{tx,rx}}{\lambda_0}} e^{\frac{j2\pi \hat{r}^T_{rx,n,m)} \bar{\nu}}{\lambda_0}},$$

where $F_{tx,\phi}$ and $F_{tx,\phi}$ are the field patterns of Tx and Rx antennas in the azimuth plane; $F_{tx,\theta}$ and $F_{tx,\theta}$ are the field patterns of Tx and Rx antennas in the zenith plane; $\hat{r}^T_{tx,n,m}$, $\hat{r}^T_{rx,n,m}$ are the spherical unit vectors. At this stage, the delay spread should be taken into account when determining the CIR. The last step in the overall process is to apply PL and shadowing on the channel coefficients. An example of the CIR obtained from the simulations is given in Fig. 3.5.

The simulation setup includes UE mobility; thus, it is crucial to maintain temporal and spatial consistency. Therefore, the consistency procedure A from [4] is utilized in this work. In this procedure, the velocity of UE is accounted for, which changes the definition of several parameters. For example, cluster delay is recalculated as

$$\tilde{\tau}_n(t_k) = \begin{cases} \tilde{\tau}_n(t_{k-1}) - \frac{\hat{r}_{rx,n}(t_{k-1})^T \bar{\nu}(t_{k-1})}{c} \Delta t, \ k > 0 \\ \tau_n(t_0) + \tau_\Delta(t_0) + \frac{d_{3D}(t_0)}{c}, \ k = 0, \end{cases} \tag{3.16}$$

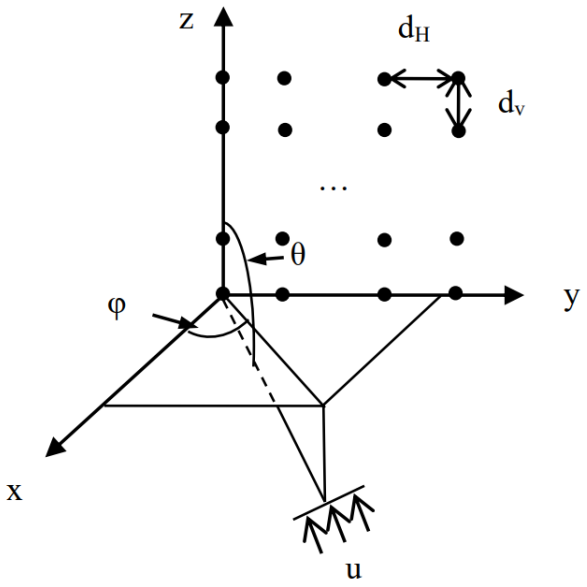

Figure 3.6 *Definition of angles and distances between elements for an antenna array of multiple rows and columns [3].*

where $\overline{\nu}(t_k)$ is the UE velocity vector; $\tau_n(t_0)$ is the cluster delay from (3.5); $\tau_\Delta(t_0) = 0$ for the LoS environment and $\min([\tau_n^{'}]_{n=1}^{N})$ for the non-LoS (NLoS) condition.

3.4 Antenna Model

In this work, an antenna array is modeled according to [4, 3], which implies that the resultant antenna pattern is represented as a superposition of element patterns. Therefore, the array factor can be written as

$$\tilde{W} = VW, \tag{3.17}$$

where

$$V(\phi, \theta) = [v_{1,1}, v_{1,2}, ..., v_{N_H,N_V}]^T \tag{3.18}$$

is the phase shift caused by the array placement and

$$W = [w_{1,1}, w_{1,2}, ..., w_{N_H,N_V}]^T \tag{3.19}$$

is the weighting factor, which determines the level of side lobes and the value of electrical down-tilt; N_H, N_V are the total number of antenna elements in horizontal and vertical planes.

A single element $w_{m,n}$ of the weighting factor W can be computed as

$$w_{m,n} = \frac{1}{\sqrt{N_H N_V}} \exp\Big[2i\pi\Big((n-1)\frac{d_V}{\lambda}\cos(\theta) + (m-1)\frac{d_H}{\lambda}\sin(\theta)\sin(\phi)\Big)\Big], \tag{3.20}$$

where $m = 1, 2, ...N_H$, $n = 1, 2, ...N_V$; ϕ and θ are the horizontal and vertical angular shifts; d_H and d_V are the distances between two antenna elements in horizontal and vertical planes.

The correlation of two different paths at the Tx is represented by a correlation matrix R. If the signal is written as

$$S(t) = [S_{1,1}, S_{1,2}, ..., S_{N_H,N_V}]^T, \tag{3.21}$$

the complex output of the antenna array at far-field is determined with the following equation:

$$y(\phi, \theta, t) = \sum_{m=1}^{N_H} \sum_{n=1}^{N_V} S_{m,n}(t) w_{m,n} E_{m,n}(\phi, \theta) = -P_E(\phi, \theta) \tilde{W}^H S(t), \tag{3.22}$$

where $E_{m,n}$ is the complex gain of the m-th column and the n-th row element, which holds

$$E_(\phi, \theta) = P_E(\phi, \theta) exp(-2\pi i((n-1)\frac{d_V}{\lambda} cos(\theta) + (m-1)\frac{d_H}{\lambda} sin(\theta) sin(\phi))), \tag{3.23}$$

and $P_E(\phi, \theta)$ is the mean power at the output of the Tx, which can be computed by taking conditional expectation of $|y(\phi, \theta, t)|^2$. Therefore, the correlation matrix R can be defined as

$$R = E(S(t)S^H(t)) = \tag{3.24}$$
$$\begin{bmatrix} R_{1,1} & R_{1,2} & ... & R_{1,N_V}...R_{1,N_V N_H} \\ R_{2,1} & R_{2,2} & ... & R_{2,N_V}...R_{2,N_V N_H} \\ ... & ... & R_{(i-1)N_V+(j-1),(k-1)N_V+(t-1)} & ... \\ R_{N_V N_H,1} & R_{N_V N_H,2} & ... & ...R_{N_V N_H,N_V N_H} \end{bmatrix}.$$

As it was mentioned, the values of cells in the matrix R determine the correlation between signals in different Tx paths. If the same correlation level ρ is assumed between the elements, then the correlation matrix becomes

$$R = E(S(t)S^H(t)) = \tag{3.25}$$
$$\begin{bmatrix} \rho & \rho & ... & \rho...\rho \\ \rho & \rho & ... & \rho...\rho \\ ... & ... & \rho & ... \\ \rho & \rho & ... & ...\rho \end{bmatrix} =$$
$$\rho(U - I) + I = \rho U + (1 - \rho)I,$$

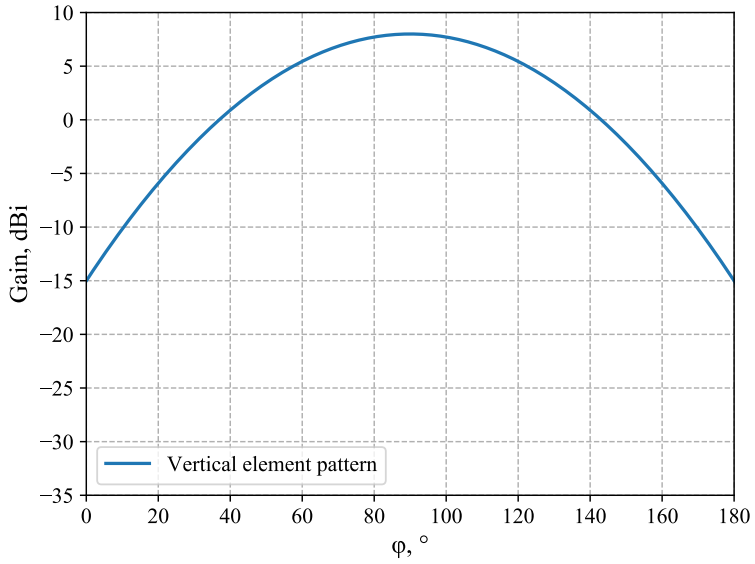

(a) Vertical element radiation pattern.

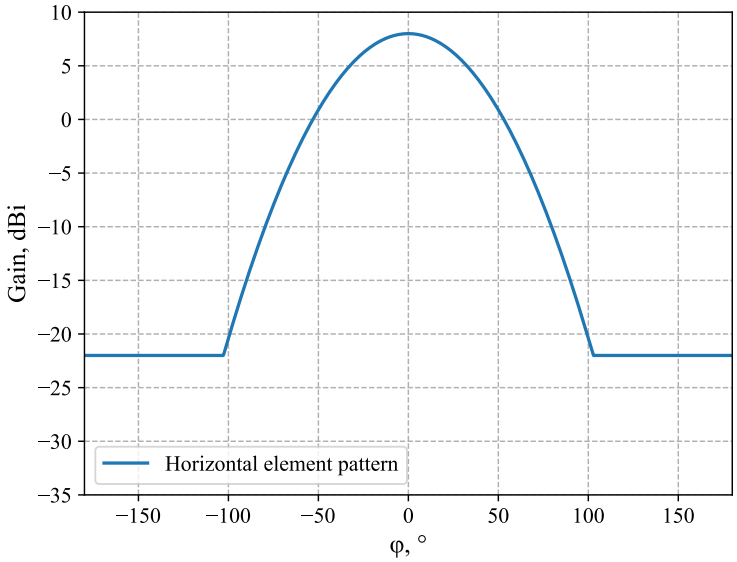

(b) Horizontal element radiation pattern.

Figure 3.7 *Vertical (a) and horizontal (b) element patterns.*

where U is the unit matrix and I the identity matrix. Using (3.25), the radiation pattern $A_A(\phi, \theta)$ can be expressed as

$$A_A(\phi,\theta) = A_E(\phi,\theta) + 10log_{10}[1 + \rho(|\sum_{m=1}^{N_H}\sum_{n=1}^{N_V} w_{m,n}v_{m,n}|^2 - 1)]. \tag{3.26}$$

If $\rho = 1$, R is the unity matrix; hence, the radiation pattern corresponds to a passive antenna. If $\rho = 0$, R becomes the identity matrix, and the radiation pattern corresponds to the radiation of an element pattern.

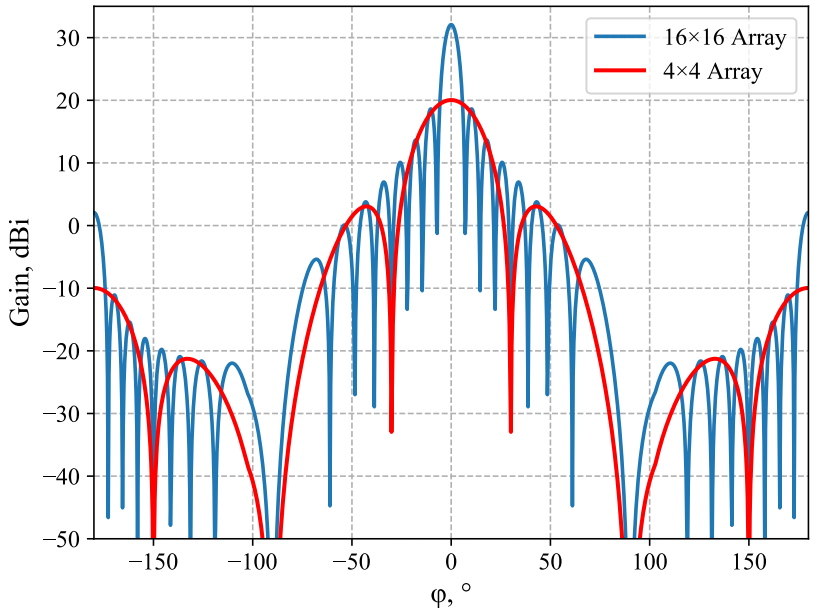

Figure 3.8 *Resultant pattern of the antenna array of 16 and 256 antenna elements.*

An element pattern A_E is given by

$$A_E(\phi, \theta) = G_E - min[-(A_{E_H}(\phi) + A_{E_V}), A_m ax], \tag{3.27}$$

where G_E is the gain of an element pattern, which is set to 8 dBi; A_{E_H} and A_{E_V} are the values of attenuation in horizontal and vertical planes; $A_m = 30$ dB is the front to back ratio. The radiation pattern of a single element is depicted in Fig. 3.7 in horizontal and vertical planes. The resultant array radiation pattern of 16 and 256 elements is shown in Fig. 3.8. With the described methodology, the HPBW of the antenna array depends on the number of antenna elements.

3.5 Blockage Model

The blockage is modeled according to [14, 17]. According to the employed model, the blockage is described as an alternating process of blocked/non-blocked states. In general, the procedure can be described via the following steps:

1. Initially, the UEs are associated using one of the considered criteria, i.e., best RSRP or the minimum number of hops.

2. The probability of LoS is calculated for each UE. According to the employed model [14], the size of the Rx is assumed to be infinitesimally small as compared to other objects. By utilizing this assumption, the width of the Rx may not be considered. This situation corresponds to the representation of a blocking area as a rectangle (see Fig. 3.9). In Fig. 3.9, the rectangular area should

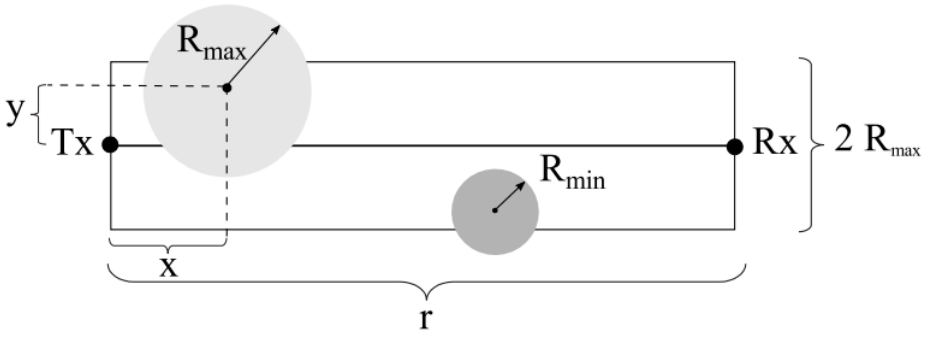

Figure 3.9 *Top view of the blockage area [14].*

include all possible blockers. The length of the area is denoted as r. In [14], it is assumed that blockers may be of different radii. The maximum radius is denoted as R_{max} while the smallest radius is denoted as R_{min} in Fig. 3.9. To determine the probability that the LoS path was blocked, the probability that at least one blocker falls into the area and blocks the LoS signal should be estimated. If the event that the radius of a blocker is insufficient to obstruct the LoS path is defined as B_0, the probability of this event is calculated as

$$Pr(B_0) = \int_{-R_{max}}^{R_{max}} f_R(y) F_R(|y|) dy, \tag{3.28}$$

where $f_R(y)$ and $F_R(y)$ are the probability density function (PDF) and the cumulative distribution function (CDF) of blocker radii where the radius is uniformly distributed in (R_{min}, R_{max}). Similarly, if the C_0 of the event that a blocker height is insufficient to obstruct the LoS path, the probability of C_0 is

$$Pr(C_0) = \int_0^r f_R(x) F_H \left(\frac{h_{tx} r - (h_{tx} - h_{rx}) x}{r} \right) dx, \tag{3.29}$$

where h_{tx} and $h_r x$ are the corresponding heights of the Tx and Rx; $f_R(x)$ is the PDF of the uniform distribution in $(0, r)$; $F_H(y)$ is the CDF of the blocker height. Assuming that blockers height and width are independent, the probability of LoS can be computed as

$$p_{nB} = p_0 + \sum_{i=1}^{\infty} p_i \prod_{j=1}^{\infty} \left(\int_{-R_{max}}^{R_{max}} f_R(y) F_R(|y|) dy + \right. \tag{3.30}$$
$$\left. \int_{-R_{max}}^{R_{max}} \int_0^r f_R(y)) (1 - F_R(|y|)) f_R(x) n \times F_H \left(\frac{h_{tx} - h_{rx} x}{r} \right) \right) dy dx,$$

where p_i, $i = 0, 1, \ldots$ are the Poisson probabilities. If it is assumed that the

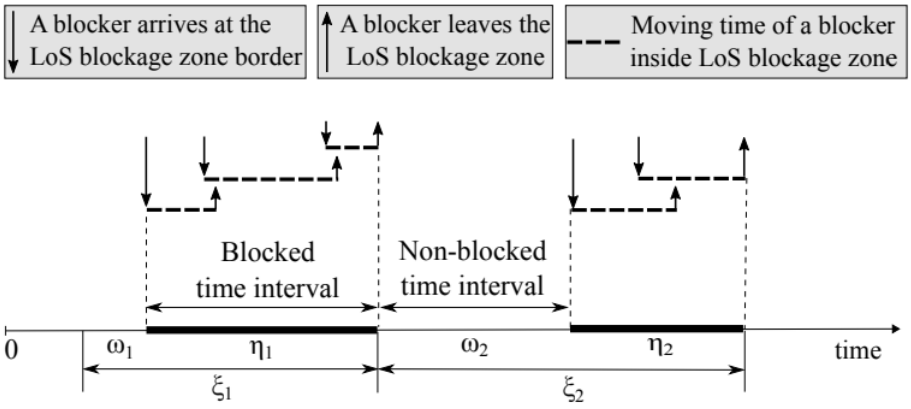

Figure 3.10 *Renewal LoS blockage process [17].*

height and width of a blocker are constants, expression (3.30) can be simplified and the probability of LoS can be expressed via the following equation:

$$p_{nB} = e^{-2R\lambda_B[x\frac{h_B-h_{rx}}{h_{tx}-h_{rx}}+R]}, \tag{3.31}$$

where h_B, R are the height and the radius of a blocker, and λ_B is the blocker density.

3. The time in blocked t_B or non-blocked t_{nB} is determined as a random variable with parameter $1/E[t_B]$ or $1/E[t_nB]$, where

$$E[t_B] = \frac{1}{\lambda_{B_t}} e^{\lambda E[T]-1}, \tag{3.32}$$

$$E[t_{nB}] = \frac{1}{\lambda_{B_t}}, \tag{3.33}$$

where λ_{B_t} is the temporal intensity of blockers, $E[T] = \frac{2r_B}{v}$ is the mean time required to cross the LoS blockage region, and v is the average velocity of blockers. In other words, the time spent in the LoS zone is represented by the renewal process, which is illustrated in Fig. 3.10. In Fig. 3.10, ω_j and ν_j correspond to the time in blocked and non-blocked states while $\xi_j = \omega_j + \nu_j$. As can be observed, the intervals corresponding to blocked and non-blocked conditions alternate, i.e. blockage period follows the LoS condition and vice-versa. In this model, the durations of non-blocked and blocked intervals are independent.

4. If the time in the previous state has expired, the state changes to the opposite, and the time is generated.

The major advantage of this model is that it is consistent in time and space. In

addition, the model is computationally efficient; thus, can be scaled to the larger blocker densities.

3.6 UE Mobility Model

As it was mentioned in section 3.1, the UEs are mobile in the considered deployment. Specifically, two UE mobility models are considered: random direction mobility (RDM) and reference point group mobility (RPGM) models [39].

The RDM captures the temporal behavior of UEs. It is an extended version of the Pearson-Rayleigh random walk model. Initially, UEs select the directions of movement randomly via the uniform distribution between 0 and 2π. Further, they move according to chosen directions with the speed of ν and for the duration of time τ, which is distributed exponentially. Typically, the speed is selected randomly via the Gaussian distribution with μ and σ for each time instant τ. In this work, the average speed is set to 3 km/h to recreate a more realistic deployment. When the UE approaches the cell edge, it changes the direction of movement to the opposite one. The traces for 2 UEs moving according to the RDM model are depicted in Fig. 3.11(a) where the trace of different UEs correspond to blue and orange colors. As can be seen from Fig. 3.11(a), after the UE starts a movement, the direction is changed after a certain period of time.

RPGM model represents another class of mobility models, i.e. group mobility [19] where each UE belongs to a group. In RPGM, UEs within a group move according to the logical center of this group, which is called a group leader. The UEs within a group are distributed randomly around a reference point. If the group leader moves with the velocity ν, the velocities of other group members deviate around this value. Therefore, every UE within a group has its own speed and direction of movement as in RDM but these parameters are derived by random deviations from that of the group leader. The maximum allowed distance of deviation r_{max} is specified as an input parameter while the direction of movement is chosen randomly in $(0, 2\pi)$. The trajectories for 10 UEs are illustrated in Fig. 3.11(b) where these UEs form a group. As can be observed, UEs have approximately the same pattern most of the time as compared to the RDM model where each UE moves independently. Moreover, the value of deviation can be controlled by adjusting the r_{max} parameter.

3.7 Implementation Details

The simulator is implemented using the discrete-event simulation (DES) method. The framework is written in Python programming language using multi-thread optimizations. The step-by-step simulation procedure can be described via the following

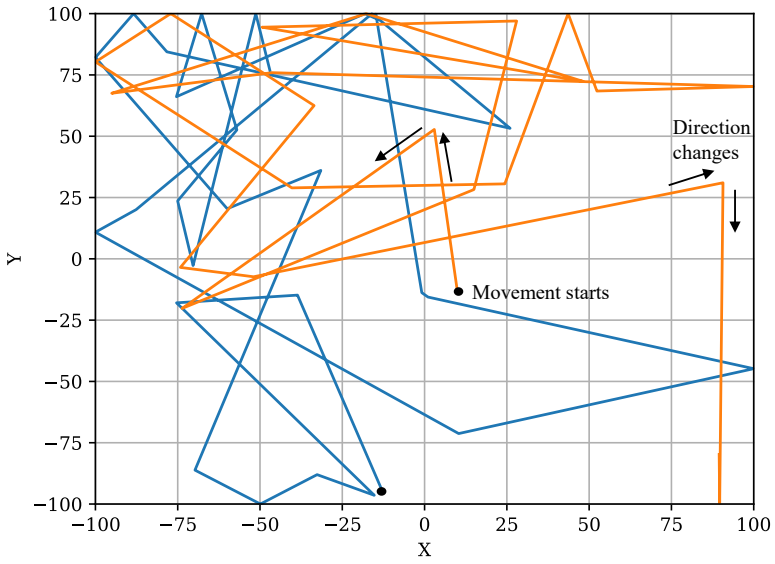

(a) UE trajectories for the RDM model.

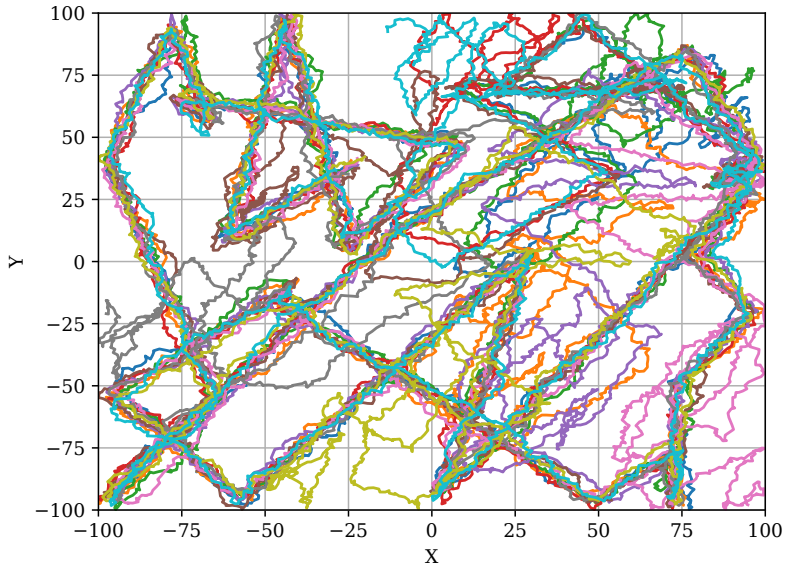

(b) UE trajectories for the RPGM model.

Figure 3.11 *UE trajectories for RDM (a) and RPGM (b) models.*

steps. At the first stage, the input parameters are specified. These parameters include antenna gains, positions of IAB nodes and the DgNB, cell size, average UE velocity, etc. Then, UEs establish associations at $t = 0$ based on the selected criterion. In this work, 2 criteria are considered: the maximum RSRP and the minimum number of hops. During the simulations, it is assumed that no misalignment happens between Tx and Rx antennas. Further, positions of UEs are updated according to the mobility model. This, in turn, causes signal degradation due to the fact that the distance from UE changes over time. Therefore, the RSRP level for each UE is continuously updated in every transmission time interval (TTI). When switching

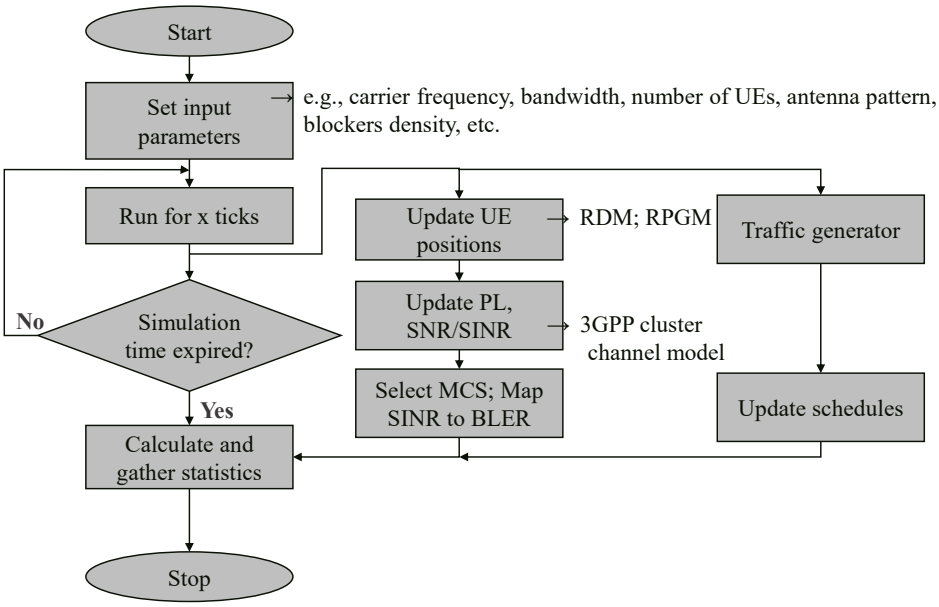

Figure 3.12 *Simplified flow chart of the developed simulation framework.*

capabilities are disabled, it is assumed that UEs are attached to the initial service nodes and no handover happens. One simulation run corresponds to $t = 1800$ s. To calculate time-averaged statistics, the method of replications is employed. The number of replications is 50.

The simplified flow chart of the developed simulation framework is provided in Fig. 3.12. The simulator consists of multiple modules following 3GPP standards, which are interconnected to each other. Initially, the input parameters are specified such as carrier frequency, cell size, antenna patterns, RA method, etc. Then, three processes are launched in time. The first one corresponds to the simulator's time generator. This process is updated each TTI and includes the conversion from the simulator's abstract ticks to the time in seconds. The second process involves the update of UE positions following one of the considered mobility models. In addition, each UE holds two time points, which need to be updated constantly. The first time instant corresponds to the blockage period, i.e. when the current state (blocked or non-blocked) ends. The second one is related to traffic generation. The traffic generation represents the next process in time, which requires a continuous update.

Depending on the state of the described modules, other processes trigger in the simulator. For example, the channel model inputs a distance between the UEs and DgNBs/IAB nodes and outputs the CIR. Then, the PL is calculated by the summation of the MPCs. It is worth noting that the summation is incoherent, i.e. the power can be increased or reduced depending on the phases of the MPCs. When the PL is known, the physical parameters such as signal-to-noise ratio (SNR) and SINR can be computed. These values are further employed to determine the

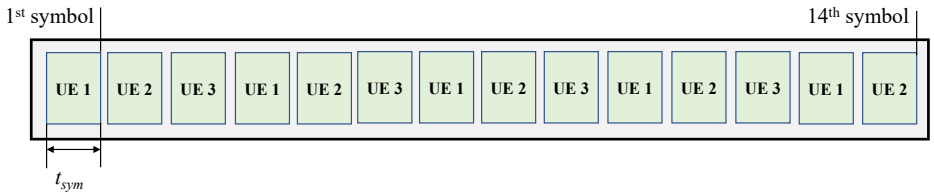

Figure 3.13 *Round-robin scheduling example for 3 UEs.*

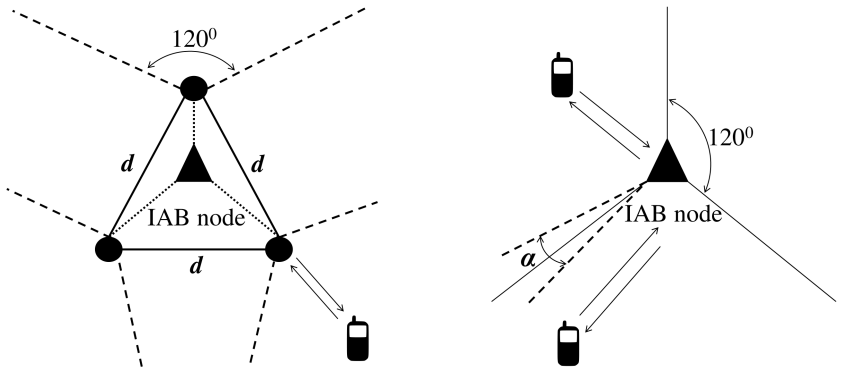

(a) Spatial diversity. (b) Angular diversity.

Figure 3.14 *Illustration of spatial (a) and angular (b) diversities.*

modulation and coding scheme (MCS) and for the block error rate (BLER) mapping depending on the selected MCS. In this procedure, MCS index table 1 from 3GPP TS 38.214 is employed [7]. The schedules are updated based on the number of active UEs. Therefore, this process depends on the traffic generator output. It is worth noting that in this work the round-robin scheduler is employed, which is the channel-unaware scheduler type. This means that after the DL and UL division coefficients were calculated, the air time is divided equally among the UEs. Then, UEs are scheduled in circular order without specific priority. To illustrate the scheduling procedure, an example is given in Fig. 3.13. In this example, it is assumed that the slot is divided among 3 UEs. In the case of channel-aware techniques, RSRP values should also be provided into the scheduler block. In the last stage, the statistics are gathered to calculate the metrics of interest.

In the simulations, the half-duplex constraint is accounted for. Thus, each time slot is divided into two parts. The methodology for obtaining the DL and UL slot division coefficients is provided in section 2.3. Different transmissions are allowed in the first and the second parts of the slot due to the half-duplex constraint. The first one corresponds to the transmissions from DgNB to UEs; DgNB to IAB node; UEs to IAB node/DgNB. The second part corresponds to the transmission from IAB node to UEs; from IAB node to DgNB; from UEs to DgNB. According to the adopted strategies, time resources are further split equally between the active UEs.

In the simulations, two approaches to mitigate inter-sector interference are ad-

dressed. Specifically, angular and spatial diversities. They are depicted in Fig. 3.14. The first method specifies the minimum angular distance between the UEs, which are associated with the adjacent sectors. According to this method, it is implied that only those UEs which have greater angular distance can be serviced simultaneously by the adjacent antenna arrays. The second method assumes the physical separation of antennas at the IAB node. In this thesis, it is considered that different antenna sectors are placed at the edges of an equilateral triangle while the IAB node is placed in the center of it to minimize cable losses.

4 Numerical Results

In this chapter, the numerical results are reported and discussed. First, inter-sector interference is estimated and two different techniques to combat it are considered. In the next section, the maximum system capacity is addressed. In addition, the proposed heuristic approach is compared with static 50/50 RA. Finally, the perspective of using multi-connectivity in IAB networks is evaluated. The system modeling parameters utilized for numerical assessments can be found in Table 3.1.

4.1 Simulator Calibration

Before analyzing the numerical results, it is required to verify the correctness of the results simulated via the developed tool. Since IAB technology is not yet employed, it is not possible to carry out the measurement procedure. Therefore, the analytical solution derived in [15] was utilized for verification. According to [15], the mean capacity for the UEs connected to the DgNB or a relay (IAB node) is expressed as

$$E[C] = \int_0^{R/2} B f_D(x) \log_2 \left(1 + \frac{R_{rx}}{N_0}\right) dx + \int_{R/2}^{R} B f_D(x) \log_2 \left(1 + \frac{R_{rx}}{N_0}\right) dx, \quad (4.1)$$

where R is the cell radius; $f_D(x)$ is the PDF of distances from UEs to the DgNB/IAB node; P_{rx} and N_0 are the received power and the noise power correspondingly. It is worth noting that the model (4.1) was developed for wireless relaying without the scope of IAB technology. Therefore, such system-specific details such as the half-duplex constrain and multi-hop relaying cannot be accounted for. However, this calibration procedure allows ensuring that the wireless part and the basic principles of the RA procedure are implemented correctly.

In addition, several simplifications should be done in the scenario to fit the analytical assumptions. Specifically, UEs are dropped randomly within the area and assumed to be static; the number of IAB nodes is reduced; the DgNB is moved to the cell center while the IAB node is dropped on a circle; blockage is disabled; simple PL calculations and static antenna gains; spectral efficiencies are calculated using the Shannon formula instead of MCS mapping. These simplifications are eliminated in further simulations. They are required only to reproduce the scenario, which is employed in [15].

The results of the calibration procedure are depicted in Fig. 4.1 where 2 cases are considered, i.e., when only the DgNB serves the cell and the DgNB with 1 IAB node. The metrics of interest are capacity per UE and aggregated capacity for UEs connected to the DgNB, capacity per UE and aggregated capacity for UEs

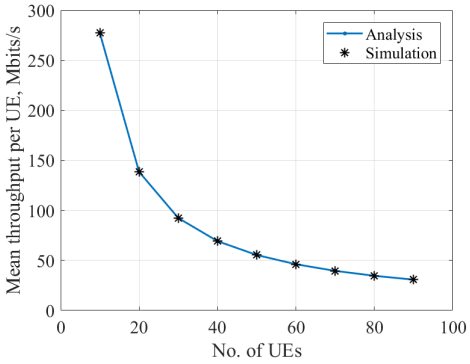

(a) Mean throughput per UE with the DgNB only.

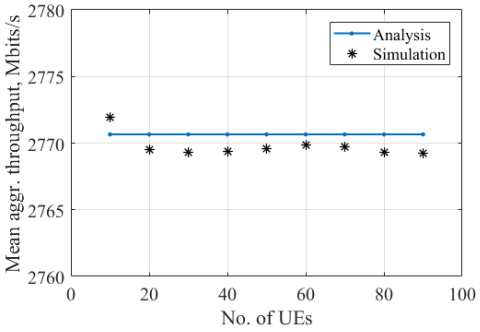

(b) Mean aggregated throughput with the DgNB only.

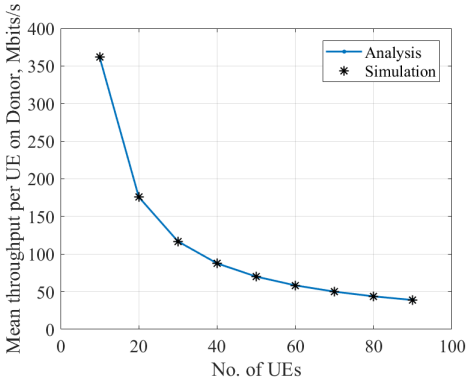

(c) Mean throughput per UE connected to the DgNB with the DgNB and 1 IAB node.

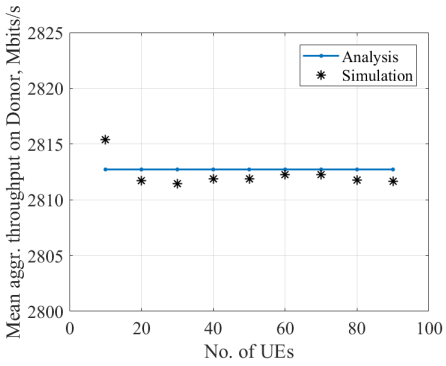

(d) Mean aggregated throughput per UE connected to the DgNB with the DgNB and 1 IAB node.

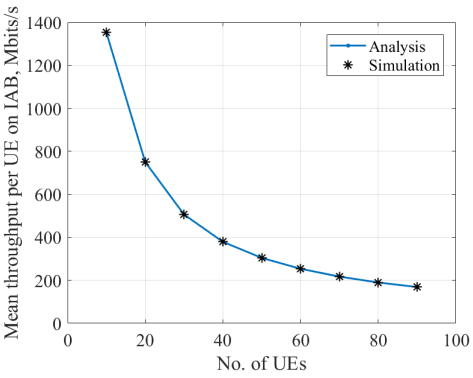

(e) Mean throughput per UE connected to the IAB node with the DgNB and 1 IAB node.

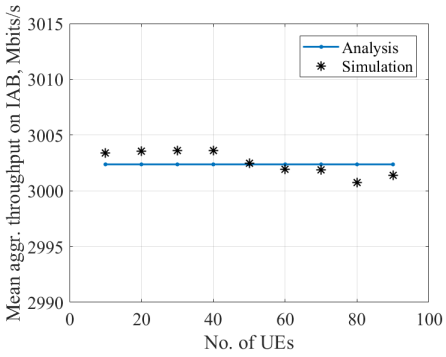

(f) Mean aggregated throughput per UE connected to the IAB node with the DgNB and 1 IAB node.

Figure 4.1 *Mean throughput per UE and mean aggregated throughput for different scenarios.*

connected to the IAB node. As can be seen, analytical and simulated throughput per UE coincides in both of the considered cases. The difference in aggregated throughput is about 1 Mbit. Therefore, it can be concluded that the wireless part and the basic principles of RA are simulated correctly.

4.2 Interference Mitigation

One of the critical design considerations, which allows the capacity of 3GPP IAB systems to be increased is the simultaneous reception by the IAB node and the DgNB. This potentially enables the utilization of the full bandwidth available in the system for transmissions at each sector of the IAB node. Hence, the first question is whether one may utilize these simultaneous transmissions or the system has to resort to a TDMA regime over IAB antenna sectors due to interference.

In the simulations, two methods to combat inter-sector interference were considered. The first one is based on the separation of different antennas of the IAB node. This can be implemented by placing antenna arrays on the vertices of the equilateral triangle while the IAB node is assumed to be the center of mass. The second approach for interference reduction in the case of simultaneous reception by different antenna sectors of the IAB node is based on scheduling. It implies that a certain angular difference is set as a threshold. Further, the scheduler assigns different time slots to those UEs, which have an angular resolution smaller than the threshold.

The averaged results for inter-sector interference are shown in Fig. 4.2. The antenna separation distance is 20 m and the angular separation is 25°. It is worth noting that the outage boundary is drawn according to the MCS table [7]. Specifically, it reflects the lowest threshold of the smallest channel quality indicator (CQI) index. It can be observed that CDFs of SINR have a difference of about 1 dB for both methods. This fact evidences that the averaged behavior of the curves is not significantly affected by interference. However, several UEs may be in outage condition regularly, which can be noticed from Fig. 4.3 with the scaled tail of the distribution. Fig. 4.3 demonstrates that smaller diversity can also reduce SI. On the other hand, when spatial diversity is $d = 5$ m or angular diversity is $\alpha = 5°$, the SI is only 1.2 times lower as compared to the situation where no diversity is utilized. Therefore, it is recommended to employ $d = 20$ m and $\alpha = 25°$ to provide SI reduction by 10 times.

Further, this effect is studied in detail to identify the desired angular and spatial antenna separations by using the SINR time series. Before discussing these results, it is crucial to mention that the angular resolution between UEs depends on the distance between service points. This is demonstrated in Fig. 4.5 where AoA is reflected as a function of the distance between the spatially separated antennas of

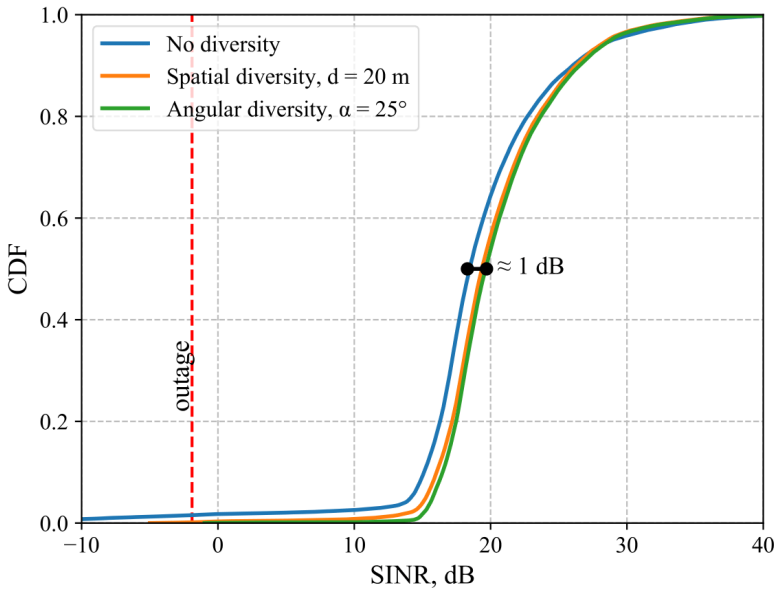

Figure 4.2 *CDF of SINR over all samples.*

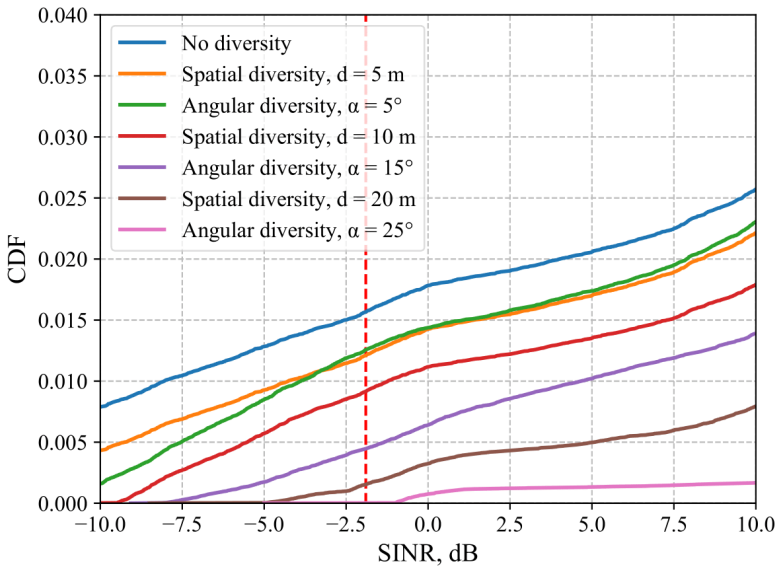

Figure 4.3 *CDF of SINR scaled from -10 dB to 10 dB.*

the IAB node. The considered distances are 20, 50, and 140 m. As can be seen in Fig. 4.5, the higher angular resolution is achieved for the higher the separation distance between sectoral antennas. According to this observation, the requirements for UE scheduling can be relaxed at IAB nodes.

The time series of SINR is depicted in Fig. 4.4(a) where 3 curves correspond to 3 different UEs. It can be seen that SNR and SINR mostly coincide in the considered period of time. However, at $t = 400$ s and $t = 1650$ s, one may observe that SINR starts to decrease. This effect indicates a significant growth of interference. The correlation between the decrease of SINR and the angular distance can be

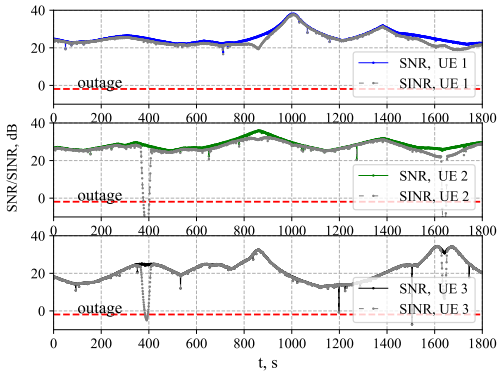

(a) SNR and SINR without antenna diversity.

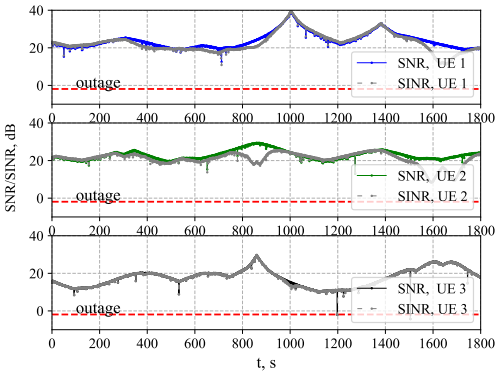

(b) SNR and SINR without antenna diversity with spatial diversity of 20 m.

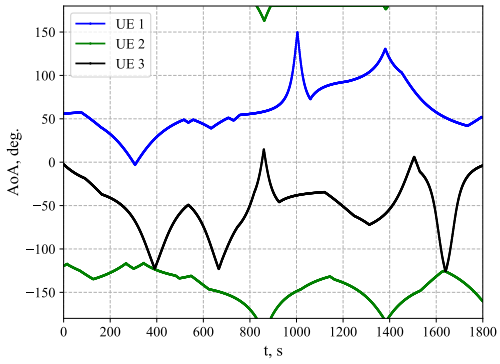

(c) AoA without antenna diversity.

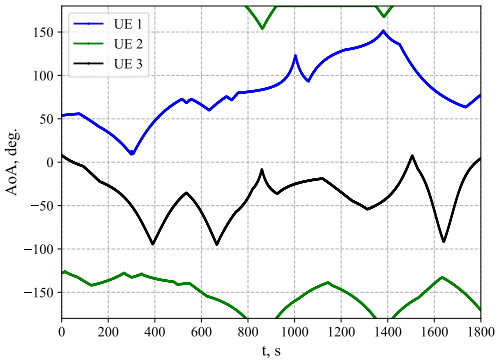

(d) AoA with 20 m antenna diversity.

Figure 4.4 *SINR as a function of time for 3 different UEs.*

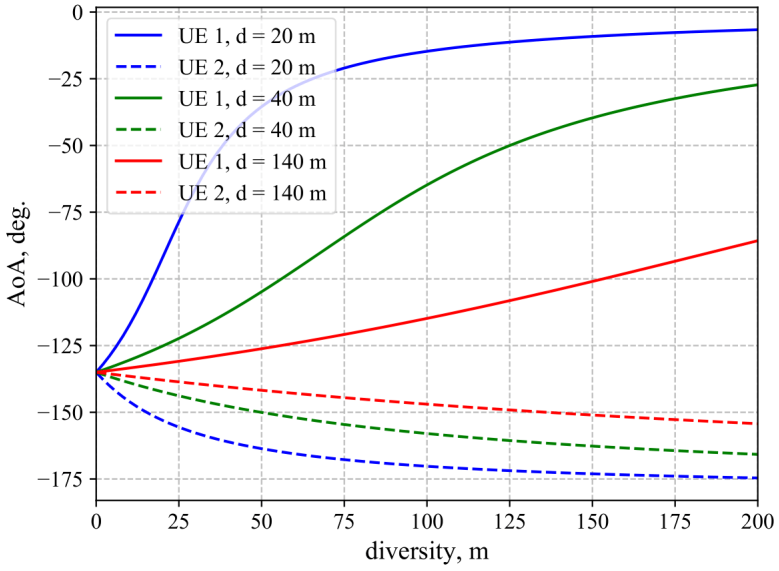

Figure 4.5 *AoA as a function of spatial diversity.*

established by considering AoA temporal behavior in Fig. 4.4(c). One may observe that time instants, at which SINR starts to decline, correspond to AoA difference of 25∘ between two UEs.

The temporal behavior of SINR and AoA with the antenna separation distance of 20 m between adjacent antenna sectors of the IAB node is provided in Fig. 4.4(b) and Fig. 4.4(d). As can be seen, an additional separation between sectoral antennas increases the angular difference between UEs. Therefore, the influence of interference on SINR can be mitigated by utilizing this method. For instance, a relatively small separation distance of 20 m allows increasing SINR by 10 dB (see Fig. 4.4(b)). On the other hand, it should be kept in mind that this value depends on the distance between the UE and the IAB node (see Fig. 4.5).

Summarizing the observations, the following conclusions can be drawn. The impact of inter-sector interference becomes crucial if the angular resolution between UEs is smaller than 25°. Therefore, either spatial diversity of at least 20 m or angular diversity of at least 25° significantly reduces this interference, which enables the avoidance of outage conditions. Hence, to utilize the full bandwidth available in the system, UEs having the angular difference of smaller than 25° should not be scheduled simultaneously.

4.3 Identifying Network Overloaded Regime

As the results of the previous section indicate, one can fully utilize system resources over all IAB sector antennas enabling simultaneous transmission and reception. Therefore, the next step is to compare the performance of the proposed RA schemes.

It is crucial to identify the achievable capacity of the system for all of the considered RA schemes. To this aim, Fig. 4.6, Fig. 4.7, and 4.8 illustrate the backlog of UEs for the 50/50, PF, and WPF schemes. The number of UEs in the results corresponding to Fig. 4.8 is 30. As can be seen, for 30 UEs backlog does not increase with session intensity, which indicates that the network is able to handle the load produced by this number of UEs. In Fig. 4.6 and 4.7, the number of UEs is increased to 60. In Fig. 4.6, the UL traffic intensity was set to 0.4 sessions per second while the DL intensity is subject to change from 0.1 to 1.4. Similar values are employed in Fig. 4.7 with the difference that the DL session arrival rate is fixed while the UL direction changes its intensity. It is worth noting that due to the symmetric nature of the considered 3GPP IAB architecture, similar conclusions can be made for the DL direction. Analyzing the presented results, one may observe that the behavior of the time-dependent curves is similar both qualitatively and quantitatively for the static and WPF allocations. Particularly, for both schemes, the backlog diverges to infinity at the DL traffic intensity of 1.0 sessions per second. In contrast, the proportional fair scheme is capable of handling the considered traffic intensities up

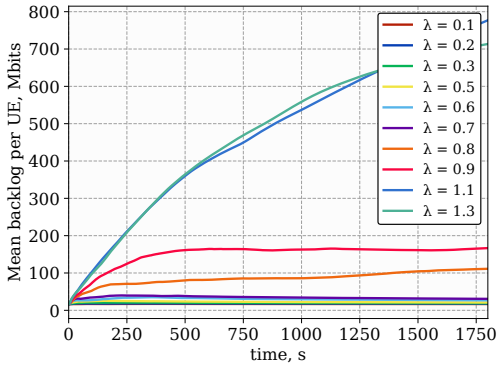

(a) Mean UE backlog for 50/50 RA scheme in the DL direction.

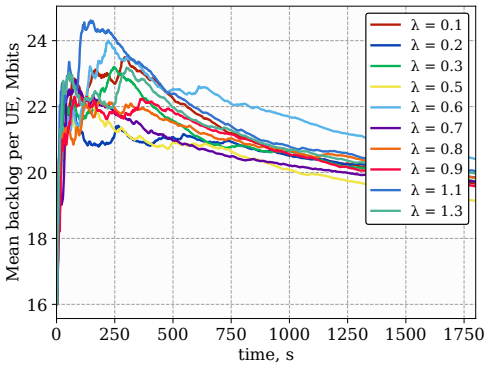

(b) Mean UE backlog for 50/50 RA scheme in the UL direction

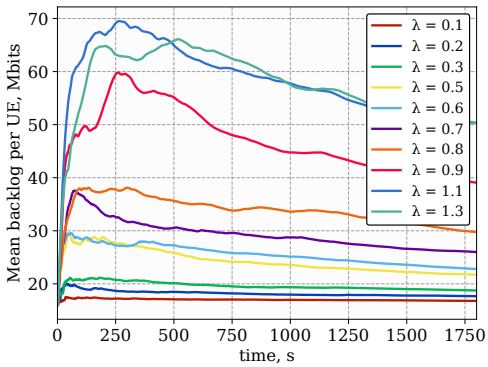

(c) Mean UE backlog for PF RA scheme in the DL direction

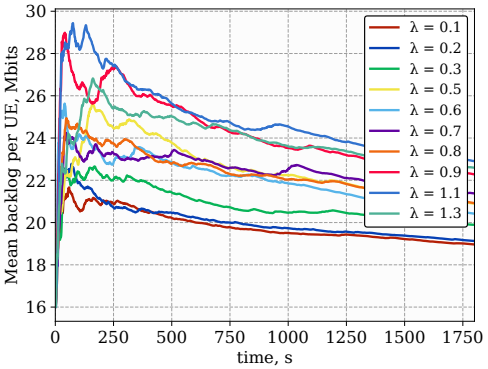

(d) Mean UE backlog for PF RA scheme in the UL direction

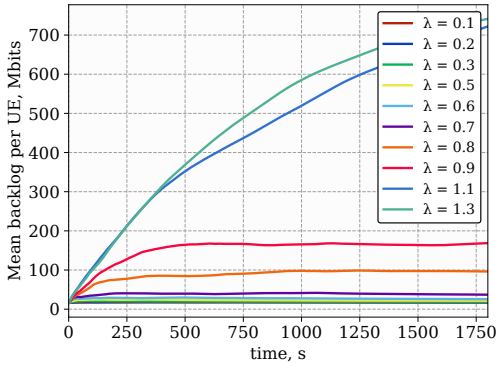

(e) Mean UE backlog for WPF RA scheme in the DL direction

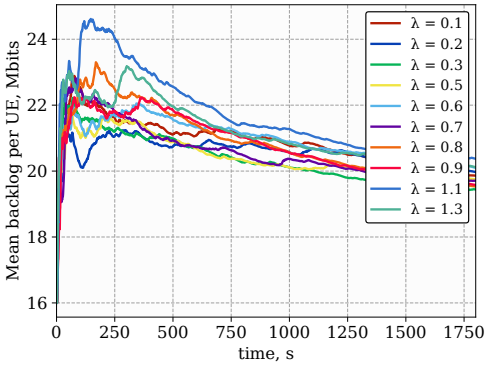

(f) Mean UE backlog for WPF RA scheme in the UL direction

Figure 4.6 *Mean backlog per UE for 60 UEs. The session arrival rate in the UL is fixed while the session arrival rate changes in the DL.*

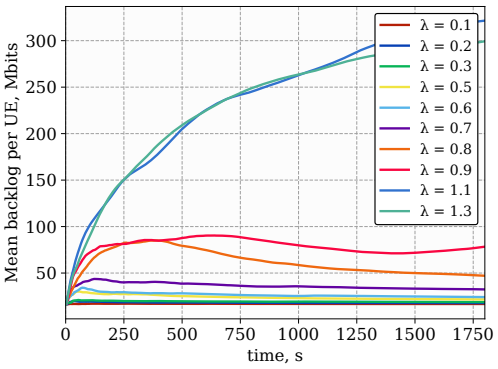

(a) Mean UE backlog for 50/50 RA scheme in the UL direction.

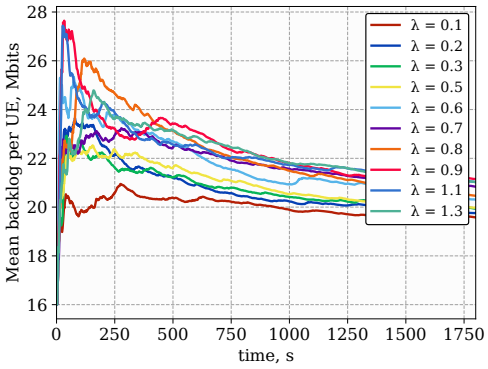

(b) Mean UE backlog for 50/50 RA scheme in the DL direction

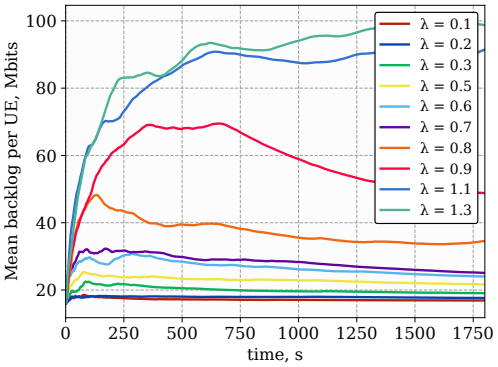

(c) Mean UE backlog for PF RA scheme in the UL direction

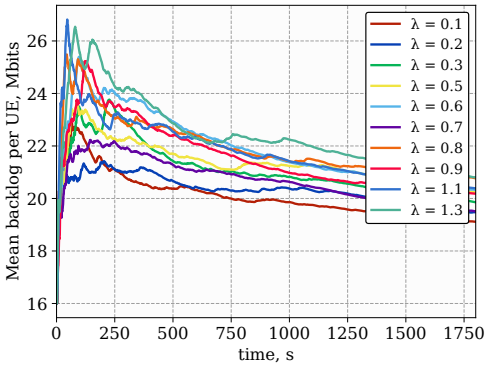

(d) Mean UE backlog for PF RA scheme in the DL direction

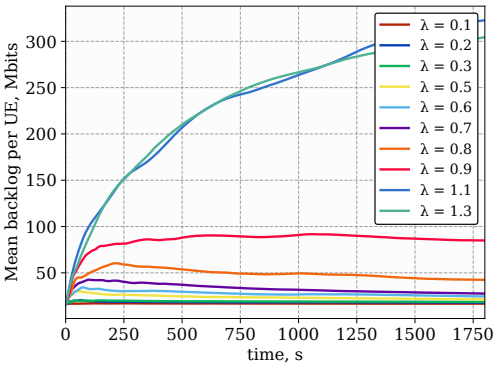

(e) Mean UE backlog for WPF RA scheme in the UL direction

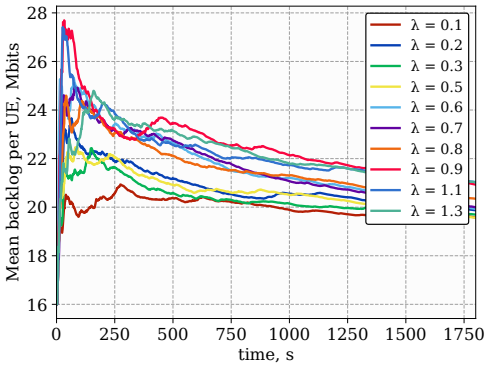

(f) Mean UE backlog for WPF RA scheme in the DL direction

Figure 4.7 *Mean backlog per UE vs time for 60 UEs. The session arrival rate in the DL is fixed while the session arrival rate changes in the UL.*

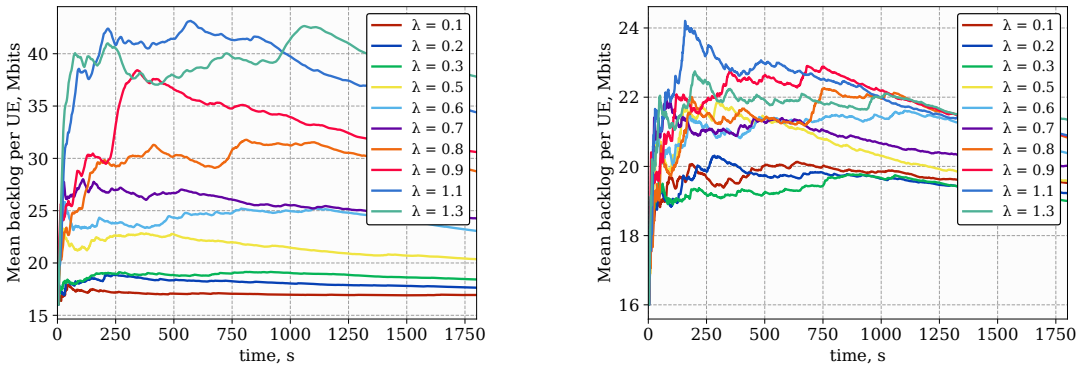

(a) Mean UE backlog for 50/50 RA scheme in the DL direction.

(b) Mean UE backlog for 50/50 RA scheme in the UL direction

Figure 4.8 *Mean backlog per UE vs time for 30 UEs. The session arrival rate in the UL is fixed while the session arrival rate changes in the DL.*

to 1.4 sessions per second. The rationale is that under high traffic conditions the WPF scheme is reduced to that of static 50/50 allocations. Similar observations can be noted in Fig. 4.7 despite the backlog is slightly higher as compared to the variable DL session arrival rate.

4.4 Resource Allocation and Multi-Hop Operations

After the capacity of the proposed RA schemes is identified, the mean throughput per UE is analyzed in a steady-state regime, i.e., when the packet losses are negligible. To this aim, Fig. 4.9 shows the mean UE throughput in the DL direction as a function of the DL traffic intensity for the fixed UL intensity of 0.4 sessions per second. As one may observe, the PF scheme shows significantly worse results for small intensities of the DL traffic. This is because the radio resources are allocated to the UL traffic for these intensities. At the same time, the WPF scheme operates close to 50/50 allocations. However, when session intensity increases further, the PF scheme provides better performance due to the fact that more resources are allocated to the DL direction. These load balancing capabilities make the PF scheme more suitable for highly loaded asymmetric traffic conditions, which frequently occur in realistic access networks. This conclusion follows from Fig. 4.9(b), which demonstrates the backlog in the DL direction. At the same time, the decreased throughput in the UL direction up to the point of 0.4 sessions per second does not affect the system performance. This can be observed in Fig. 4.10(b), which illustrates the mean UE backlog in the UL direction, which indicates that the backlog corresponding to the PF scheme is similar to the other schemes.

One of the critical design parameters for half-duplex IAB architecture is the amount of memory that needs to be supported at IAB nodes for the temporary storage of packets. To assess the effect of the considered RA schemes on this design

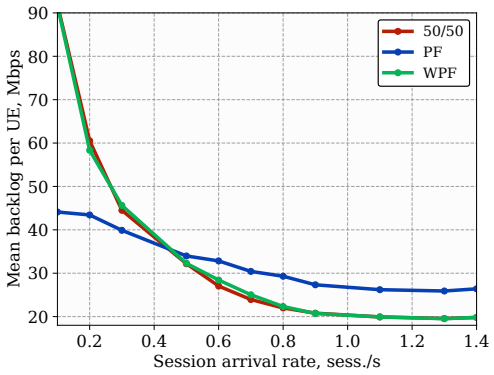

(a) Throughput for the considered RA schemes in the DL direction.

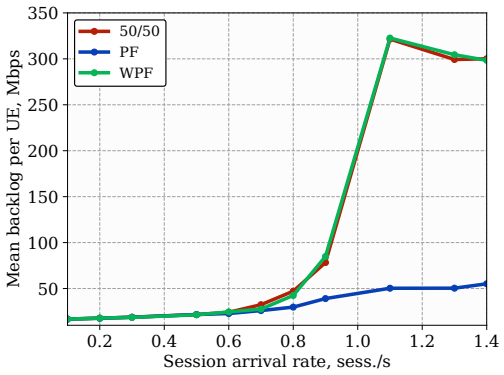

(b) Backlog for the considered RA schemes in the DL direction.

Figure 4.9 *Mean UE throughput and backlog as functions of session intensity in the DL direction for the case of fixed session arrival rate in the UL.*

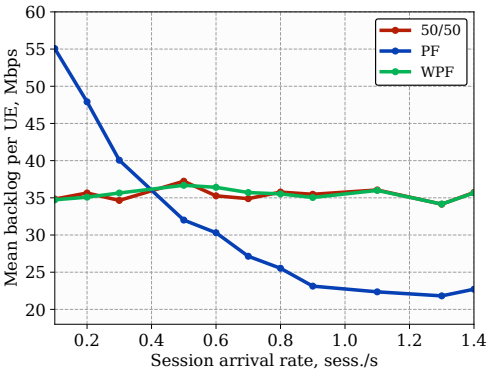

(a) Throughput for the considered RA schemes in the UL direction.

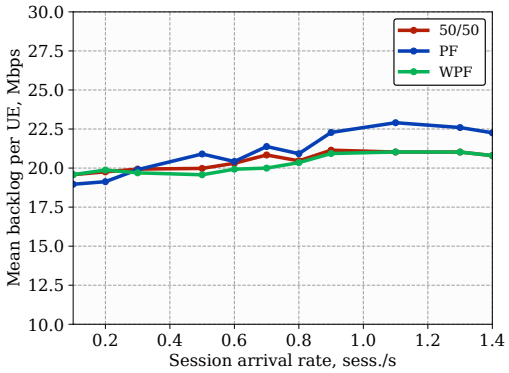

(b) Backlog for the considered RA schemes in the UL direction.

Figure 4.10 *Mean UE throughput and backlog as functions of session intensity in the UL direction for the case of fixed session arrival rate in the DL.*

parameter, the average UE backlog as a function of the DL traffic intensity is considered in Fig. 4.9(b) where the UL session intensity is constant at 0.4. Analyzing these data, one may observe that the proposed PF scheme drastically reduces the amount of buffering space required at IAB relay nodes. Specifically, the PF RA scheme outperforms other schemes by 250 Mbits while the impact in the opposite direction is negligible.

As can be seen in Fig. 4.10(b), which indicates the backlog in the UL direction, the backlog for the PF scheme is similar to the other schemes. This is because the network is able to handle the load produced by UEs with the session arrival rate of 0.4 sessions per second even with a lower rate as compared to the one, which is

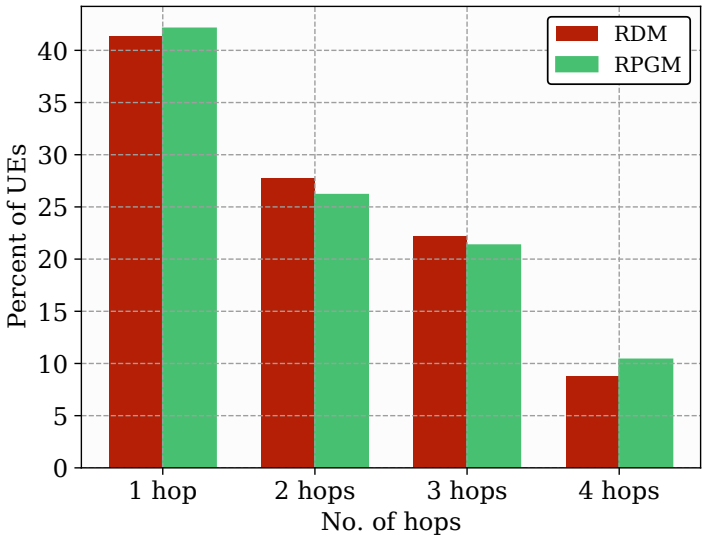

(a) Mean number of hops with the RSRP-based path selection strategy.

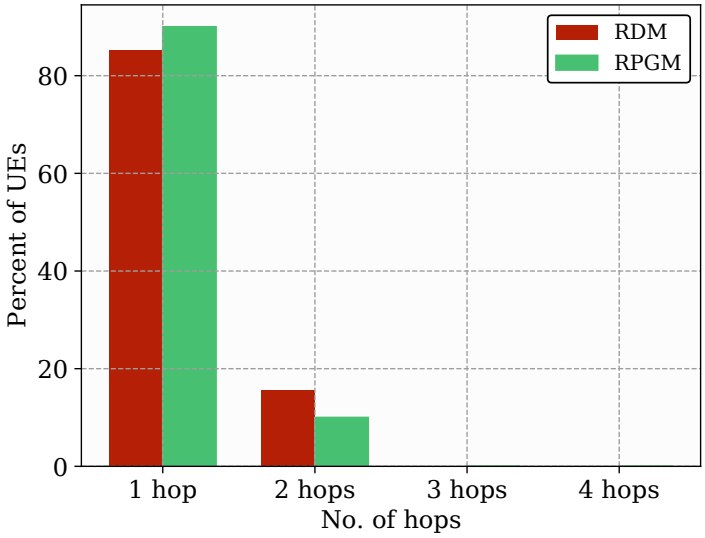

(b) Mean number of hops with the path selection strategy based on the minimum number of hops.

Figure 4.11 *Mean number of hops for the considered multi-hopping strategies.*

obtained as a result of 50/50 or WPF allocations. Speaking in absolute numbers the difference reaches 3 times for 1.0 intensity of session arrivals when all three considered RA schemes lead to non-overloaded system behavior.

The next step in this study is to address the multi-hopping schemes. Fig. 4.11 demonstrates the mean number of hops in the network for the considered multi-hopping schemes averaged over different session intensities for the RDM and RPGM models. As follows from Fig. 4.11(a), less than half of the UEs select a single-hop topology due to the RSRP association strategy. However, for the minimum number of hops, the percent of UEs connected to the DgNB reaches 90 % because the UEs

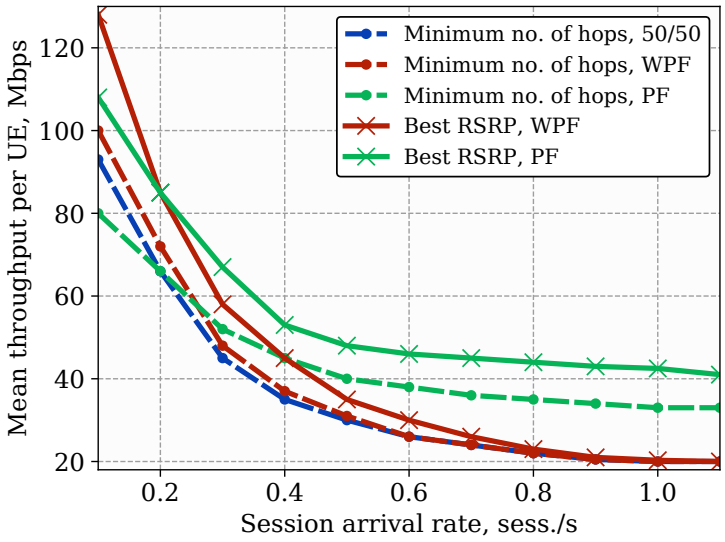

Figure 4.12 *Mean throughput per UE as functions of session intensity for the considered RA and multi-hopping schemes.*

are forced to connect to the DgNB if it is available despite the channel quality.

Then, the multi-hopping strategies are analyzed jointly with the RA schemes. The results are illustrated in Fig. 4.12, where the UL session arrival rate is fixed to 0.2 sessions per second. In this setup, the considered functionalities are utilized without the multi-connectivity support and for the single beam scenario. As it was identified in the previous section, the session intensity of 0.2 corresponds to the non-overloaded network regime. Referring to the results, it can be noted that the association scheme based on the minimum number of hops provides the lowest throughput, which happens due to the lower channel quality. Moreover, the results for the 50/50 and WPF RA schemes almost coincide. The WPF scheme converges to the 50/50 division approach as it provides the coefficients equal to 0.5 most of the time.

4.5 Multi-Connectivity and Multi-Beam Features

The next goal is to study the effects of multi-connectivity schemes. Particularly, in Fig. 4.13, the mean throughput per UE is demonstrated for the two considered mobility models: purely stochastic RDM, and clustered RPGM. The throughput is presented as a function of the intensity of blockers in the environment. In this setup, the UL and DL traffic intensities are set to 0.4, which ensures that the system is not overloaded. It is worth noting that the identified conclusions remain valid for other traffic intensities.

Starting the analysis with a commonly utilized RDM mobility model resulting in uniform distribution of active UE in the coverage area at all times. One can first

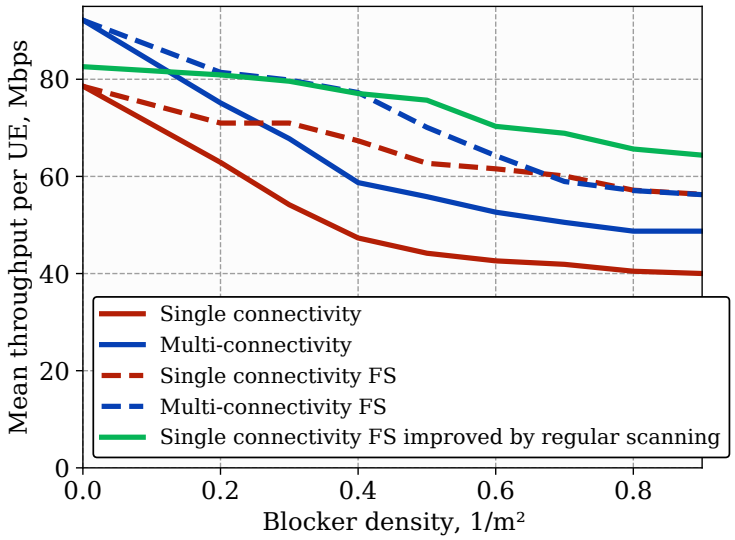

(a) Mean throughput per UE.

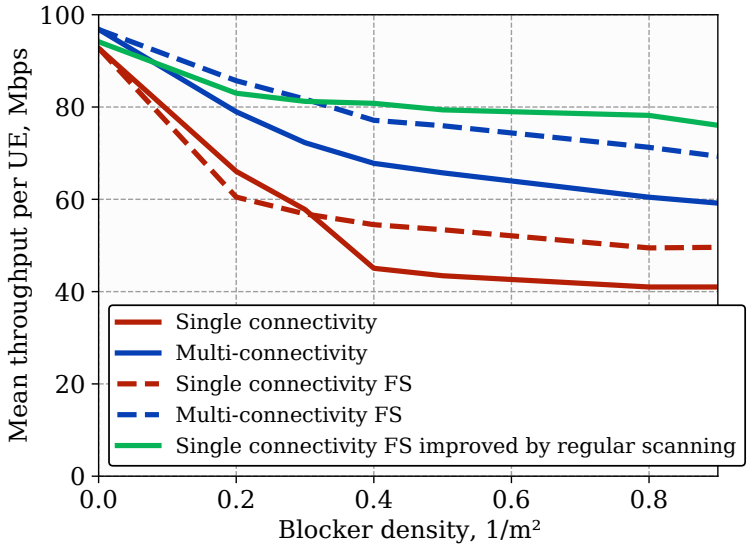

(b) Mean backlog per UE.

Figure 4.13 *Mean throughput per UE as a function of blocker density with and without multi-connectivity operation for RDM 4.13(a) and RPGM 4.13(b) models.*

notice that the FS mechanism improves the throughput per UE irrespective of the number of the maintained connections. It is worth mentioning that this is a natural behavior in presence of blockers as the latter leads to either outage or immediate degradation of the SINR. Allowing UEs to switch to backup links efficiently improves the throughput.

The number of allowed links to be used for data transmission heavily depends on the blocker intensity. As one may observe, the multi-connectivity scheme always outperforms a single connectivity scheme. However, this effect is noted for low blocker intensities. The rationale is that in addition to performance improvement

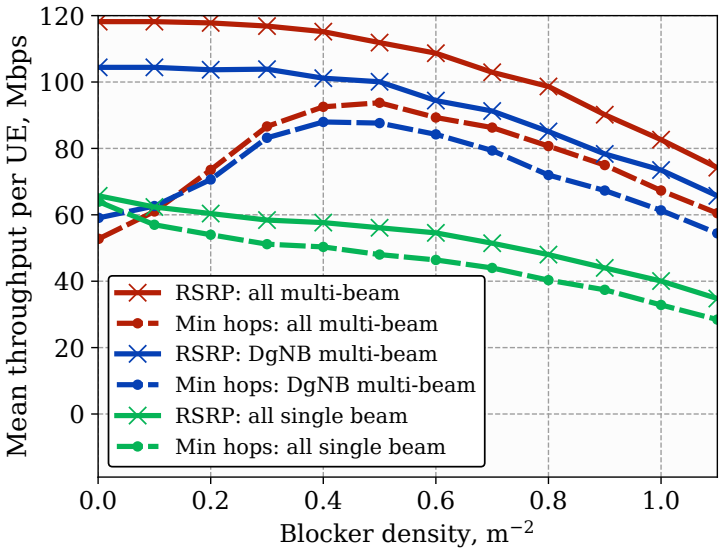

(a) Mean throughput per UE.

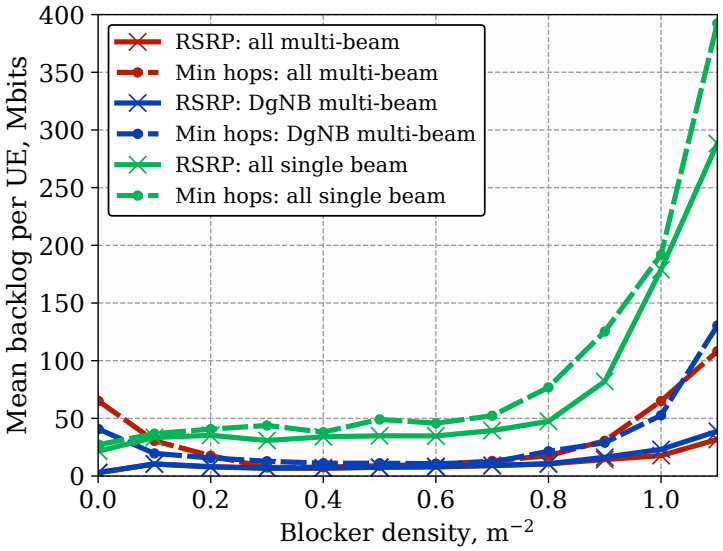

(b) Mean backlog per UE.

Figure 4.14 *Mean throughput and backlog per UE as a function of blockers density for different association schemes with and without multi-beaming in case of RDM.*

due to the presence of a backup link in case of blockage, the usage of more than a single link leads to a more uniform load distribution across the DgNB and IAB nodes. This is explained by clusterization, which is common in a purely stochastic process [9]. This effect is addressed in more detail when analyzing the results of the RPGM mobility model.

Another noted effect is that the single-connectivity scheme with FS capabilities outperforms multi-connectivity in scenarios with moderate and high blocker intensities. The FS is a dynamic procedure that scans the environment in case of link blockage. Therefore, the throughput increases due to the fact that the scheme selects

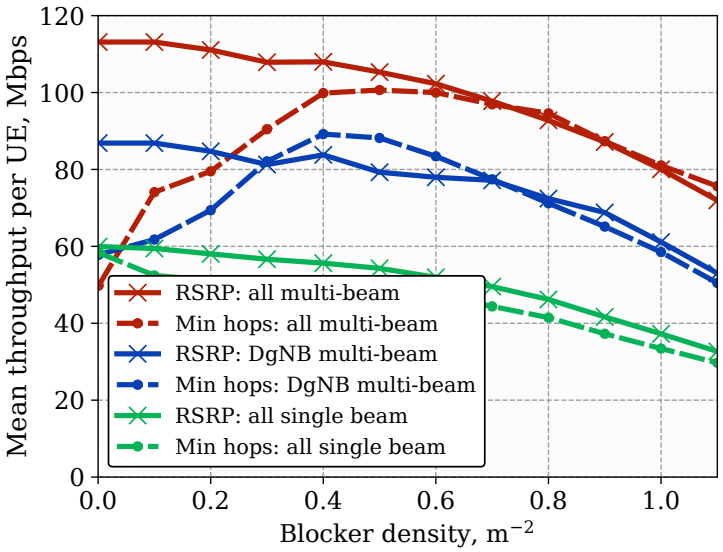

(a) Mean throughput per UE.

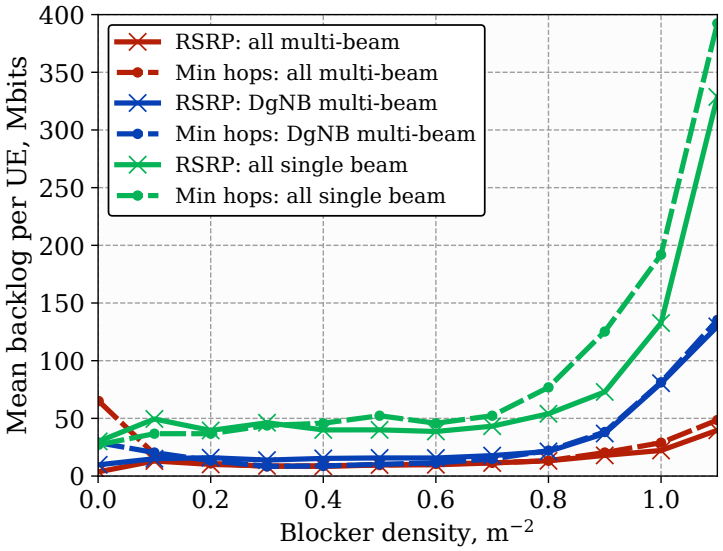

(b) Mean backlog per UE.

Figure 4.15 *Mean throughput 4.14(a) and backlog 4.14(b) per UE as a function of blockers density for different association schemes with and without multi-beaming in case of RPGM.*

a currently non-blocked IAB node or DgNB. Enabling more dynamics, i.e., allowing to regularly monitor the environment for service entity, improves the SINR. This conclusion follows from the latter considered scheme that shows that the throughput for higher blocker intensities is higher with FS functionality even if the system operates in a single connectivity mode.

Further, the performance of the RPGM model is investigated. This model introduces UE clusterization in the considered deployment. It should be noted that the conclusions related to the positive effect of FS remain true. Specifically, both single and multi-connectivity schemes with FS capabilities outperform their counterparts

without FS for moderate and high blocker intensities. On the other hand, for low blocker intensity, the dynamic feature may even perform worse. The rationale is that the distance to the service entity, to which UE switches, is on average much greater than for the RDM mobility model.

Another property, which is affected by the distance is the following. Single connectivity with FS and multi-connectivity schemes without FS outperform the single connectivity mechanism without FS. Note that in moderate- and high- dense crowds the performance can be drastically improved by a regular update of an operational link. As it was demonstrated earlier, this conclusion also holds true for the RDM mobility model implying that dynamic links have to be essential for 3GPP IAB architecture. In addition, single-connectivity schemes lead to the tree topology, which is easier to control as compared to the directed acyclic graph, which is formed if a multi-connectivity setup is utilized.

The last advanced functionality addressed in this thesis is multi-beam operation at the DgNB and IAB nodes. The mean throughput and backlog per UE as functions of blocker density for different multi-hop strategies with and without multi-beam operation are depicted in Fig. 4.14 for the RDM model and in Fig. 4.15 for the RPGM model. The session arrival rate in the UL and DL directions coincide and equal 0.5 sessions per second. In these results, single connectivity with FS improved by the regular scanning is employed as it demonstrates the best results in the previous study.

The most notable observation reads in a significant positive effect of multi-beaming. Quantifying the impact, multi-beam operation at the DgNB enhances the UE throughput by around $50-70$ % depending on the intensity of the blocker. Moreover, the backlog for multi-beam scenarios is much lower as compared to the all-single beam case. The addition of multi-beaming support to IAB nodes improves the performance further by $10-15$ %. Therefore, it can be concluded that the presence of multi-beam functionality is crucial for the DgNB while IAB nodes can be single beam and still deliver appropriate throughput. Moreover, this configuration is cheaper to deploy as compared to the all-multi-beam case.

The path selection schemes are compared in Fig. 4.14 and 4.15. As can be seen, the scheme based on the minimum number of hops demonstrates much lower throughput at the beginning. However, it improves with higher blocker density. This happens because of the blockage of the UE-DgNB link, which forces the UEs to choose other paths. This effect, in turn, allows unloading the DgNB. As there are multiple resource pools in the multi-beam setup, the throughput increases as more UEs select other association points instead of the DgNB. After the blocker density of 0.5, the curves, which correspond to the minimum number of hops strategy with multi-beam functionality start to behave similarly to the best RSRP case. The

impact of unloading is even more beneficial for the RPGM model. For example, in Fig. 4.15, the curve corresponding to the minimum number of hops scheme and multi-beaming starts to coincide with the curve corresponding to the best RSRP scheme after the blocker density of 0.5 m^{-2}. The explanation is that load balancing is more important for the group mobility models where UEs tend to occupy one location.

5 Conclusions

IAB technology allows reducing the deployment cost by enabling wireless backhaul and simplified architecture. It is characterized by intensive reuse of functions and interfaces at the backhaul, which were initially defined for the access links. Moreover, IAB relaying promises to provide both throughput gain and coverage extension. While the coverage extension functions were investigated in the up-to-date literature, the throughput benefits in the context of IAB deployments remain unclear.

One of the crucial design options, which enables the capacity improvement of 3GPP IAB networks is the simultaneous transmission and reception at the IAB nodes. This feature allows employing the full bandwidth, which is available in the system, and providing simultaneous service to access and backhaul links. After the resources are fully utilized, the throughput can be increased further by employing such advanced functionalities as multi-beaming, multi-connectivity, multi-hopping, and dynamic RA. However, the impact of these operations on the system performance in the context of IAB technology is unclear as it has not been addressed in the literature.

In this work, the system-level simulator for IAB networks was developed and calibrated. Using this tool, the effect of simultaneous reception by adjacent sectors of the IAB nodes on the SINR was assessed. Moreover, the impact of such functionalities as multi-beaming, multi-connectivity, multi-hopping, and dynamic RA was quantified. The main conclusions of this work can be summarized as follows:

- On average, the impact on the SINR from the simultaneous reception is relatively small and varies around 1 dB. However, certain UEs may experience outage conditions regularly. To alleviate these, either spatial or angular diversity can be utilized. Specifically, the angular distance of 25° is sufficient to mitigate SI. A significant reduction in SI can be achieved by employing the antenna separation distance of at least 20 m. By utilizing these methods, one can identify the target levels of spatial and angular diversities suitable for given deployment restrictions.

- The dynamic RA is beneficial in IAB networks despite the asymmetry introduced by the half-duplex constraint. Specifically, the capacity boost from dynamic RA over multi-hop topologies reaches 10-30 %.

- The throughput increase due to the use of multi-hopping is noticeable even without the multi-connectivity and multi-beam operational regime of the DgNB, which allows operators to deploy low-cost setups even at an early stage of market penetration.

- Multi-connectivity functionality with advanced link switching schemes enables capacity gains from 10 to 40 % depending on the density of blockers. Moreover, advanced link selection schemes allow distributing the load among IAB nodes and DgNBs evenly. Regular update of better available links allows enforcing self-load balancing. Additionally, this reflects the mobility of UEs in the service area. Therefore, mmWave access systems may not require additional load balancing techniques.

- Multi-beam operation leads to higher performance irrespective of other system parameters. However, the major gain provided by this functionality is due to multi-beaming at the DgNB. Therefore, this provides a trade-off between the deployment cost and the system performance.

The simulation tool described in this thesis accounts for the IAB-specific details according to 3GPP. It allows accurately studying the impact of system dynamics on system performance. Moreover, the flexibility of the simulator enables the evaluation of different RA techniques, path selection strategies, switching schemes, etc., which can be useful for operators on the network design stage. For example, one may employ this tool to identify the divergence time of the system given the RA.

References

[1] 3GPP. “Initial access and network setup for IAB”. In: *3GPP TSG RAN WG2 Meeting R2-1912706* (2019).

[2] 3GPP. “NR; Multi-connectivity (Release 15)”. In: *3GPP TS 37.340 V15.0.0* (2018).

[3] 3GPP. “Study of AAS Base Station (Release 12)”. In: *3GPP TR 37.840 V1.0.0* (2012).

[4] 3GPP. “Study on channel model for frequencies from 0.5 to 100 GHz (Release 15)”. In: *3GPP TR 138.901 V15.0.0* (2018).

[5] 3GPP. “Study on Integrated Access and Backhaul (Release 16)”. In: *3GPP TR 38.874 V16.0.0* (2018).

[6] 3GPP. “System Level Simulation Results for IAB Networks”. In: *3GPP TSG-RAN WG1 Meeting RAN1 95 R1-1813418* (2018).

[7] 3GPP. “Technical Specification Group Radio Access Network; NR; Physical layer procedures for data (Release 16)”. In: *3GPP TS 38.214 V16.4.0* (2020).

[8] Mamta Agiwal, Abhishek Roy, and Navrati Saxena. “Next Generation 5G Wireless Networks: A Comprehensive Survey”. In: *IEEE Communications Surveys Tutorials* 18.3 (2016), pp. 1617–1655.

[9] David Aldous. *Probability approximations via the Poisson clumping heuristic*. Vol. 77. Springer Science & Business Media, 2013.

[10] Muhammad Amjad, Leila Musavian, and Mubashir Husain Rehmani. “Effective capacity in wireless networks: A comprehensive survey”. In: *IEEE Communications Surveys & Tutorials* 21.4 (2019), pp. 3007–3038.

[11] Ramez Askar et al. “Interference Handling Challenges toward Full Duplex Evolution in 5G and Beyond Cellular Networks”. In: *IEEE Wireless Communications* 28.1 (2021), pp. 51–59.

[12] Qingqing Cheng, Zhiqiang Wei, and Jinhong Yuan. “Deep Reinforcement Learning-based Spectrum Allocation and Power Management for IAB Networks”. In: *2021 IEEE International Conference on Communications Workshops (ICC Workshops)*. 2021, pp. 1–6.

[13] Abdurrahman Fouda et al. “Interference management in UAV-assisted integrated access and backhaul cellular networks”. In: *IEEE Access* 7 (2019), pp. 104553–104566.

[14] Margarita Gapeyenko et al. “Analysis of human-body blockage in urban millimeter-wave cellular communications”. In: *2016 IEEE International Conference on Communications (ICC)*. IEEE. 2016, pp. 1–7.

[15] Margarita Gapeyenko et al. “Comparing Capacity Gains of Static and UAV-Based Millimeter-Wave Relays in Clustered Deployments”. In: *2020 IEEE International Conference on Communications Workshops (ICC Workshops)*. IEEE. 2020, pp. 1–7.

[16] Margarita Gapeyenko et al. “On the degree of multi-connectivity in 5G millimeter-wave cellular urban deployments”. In: *IEEE Transactions on Vehicular Technology* 68.2 (2018), pp. 1973–1978.

[17] Margarita Gapeyenko et al. “On the temporal effects of mobile blockers in urban millimeter-wave cellular scenarios”. In: *IEEE Transactions on Vehicular Technology* 66.11 (2017), pp. 10124–10138.

[18] Amitabha Ghosh et al. “5G Evolution: A View on 5G Cellular Technology Beyond 3GPP Release 15”. In: *IEEE Access* 7 (2019), pp. 127639–127651.

[19] Xiaoyan Hong et al. “A group mobility model for ad hoc wireless networks”. In: *Proceedings of the 2nd ACM international workshop on Modeling, analysis and simulation of wireless and mobile systems*. 1999, pp. 53–60.

[20] Yiming Huo et al. “Multi-Beam Multi-Stream Communications for 5G and beyond Mobile User Equipment and UAV Proof of Concept Designs”. In: *2019 IEEE 90th Vehicular Technology Conference (VTC2019-Fall)*. 2019, pp. 1–5.

[21] Muhammad Nazmul Islam et al. “Investigation of performance in integrated access and backhaul networks”. In: *IEEE INFOCOM 2018-IEEE Conference on Computer Communications Workshops (INFOCOM WKSHPS)*. IEEE. 2018, pp. 597–602.

[22] Suhanya Jayaprakasam et al. “Robust beam-tracking for mmWave mobile communications”. In: *IEEE Communications Letters* 21.12 (2017), pp. 2654–2657.

[23] Elham Kalantari et al. “User association and bandwidth allocation for terrestrial and aerial base stations with backhaul considerations”. In: *2017 IEEE 28th Annual International Symposium on Personal, Indoor, and Mobile Radio Communications (PIMRC)*. IEEE. 2017, pp. 1–6.

[24] Yu-Ngok Ruyue Li et al. “Beam Management in Millimeter-Wave Communications for 5G and Beyond”. In: *IEEE Access* 8 (2020), pp. 13282–13293.

[25] Yilin Li et al. “Integrated access and backhaul optimization for millimeter wave heterogeneous networks”. In: *arXiv preprint arXiv:1901.04959* (2019).

[26] David López-Pérez et al. “Towards 1 Gbps/UE in cellular systems: Understanding ultra-dense small cell deployments”. In: *IEEE Communications Surveys & Tutorials* 17.4 (2015), pp. 2078–2101.

[27] Anna Łukowa and Venkatkumar Venkatasubramanian. “Dynamic In-band Self-backhauling for 5G Systems with Inter-cell Resource Coordination”. In: *International Journal of Wireless Information Networks* 26.4 (2019), pp. 319–330.

[28] Matteo Pagin et al. “Resource Management for 5G NR Integrated Access and Backhaul: a Semi-centralized Approach”. In: *IEEE Transactions on Wireless Communications* (2021), pp. 1–1.

[29] Joan Palacios, Danilo De Donno, and Joerg Widmer. “Tracking mm-Wave channel dynamics: Fast beam training strategies under mobility”. In: *IEEE INFOCOM 2017-IEEE Conference on Computer Communications*. IEEE. 2017, pp. 1–9.

[30] José Perdomo et al. “User Performance in a 5G Multi-connectivity Ultra-Dense Network City Scenario”. In: *2020 IEEE 45th Conference on Local Computer Networks (LCN)*. 2020, pp. 195–203.

[31] Vitaly Petrov et al. “Dynamic multi-connectivity performance in ultra-dense urban mmWave deployments”. In: *IEEE Journal on Selected Areas in Communications* 35.9 (2017), pp. 2038–2055.

[32] Michele Polese et al. “Distributed path selection strategies for integrated access and backhaul at mmWaves”. In: *2018 IEEE Global Communications Conference (GLOBECOM)*. IEEE. 2018, pp. 1–7.

[33] Michele Polese et al. “End-to-end simulation of integrated access and backhaul at mmWaves”. In: *2018 IEEE 23rd International Workshop on Computer Aided Modeling and Design of Communication Links and Networks (CAMAD)*. IEEE. 2018, pp. 1–7.

[34] Michele Polese et al. “Integrated Access and Backhaul in 5G mmWave Networks: Potential and Challenges”. In: *IEEE Communications Magazine* 58.3 (2020), pp. 62–68.

[35] Sundeep Rangan, Theodore S Rappaport, and Elza Erkip. “Millimeter-wave cellular wireless networks: Potentials and challenges”. In: *Proceedings of the IEEE* 102.3 (2014), pp. 366–385.

[36] Theodore S. Rappaport et al. “Millimeter Wave Mobile Communications for 5G Cellular: It Will Work!” In: *IEEE Access* 1 (2013), pp. 335–349.

[37] Theodore S Rappaport and Sijia Deng. “73 GHz wideband millimeter-wave foliage and ground reflection measurements and models”. In: *2015 IEEE International Conference on Communication Workshop (ICCW)*. IEEE. 2015, pp. 1238–1243.

[38] Azad Ravanshid et al. “Multi-connectivity functional architectures in 5G”. In: *2016 IEEE International Conference on Communications Workshops (ICC)*. 2016, pp. 187–192.

[39] Radhika Ranjan Roy. *Handbook of mobile ad hoc networks for mobility models*. Vol. 170. Springer, 2011.

[40] Chiranjib Saha and Harpreet S Dhillon. “Millimeter Wave Integrated Access and Backhaul in 5G: Performance Analysis and Design Insights”. In: *IEEE Journal on Selected Areas in Communications* 37.12 (2019), pp. 2669–2684.

[41] Malcolm M Sande, Mduduzi Comfort Hlophe, and Bodhaswar T Maharaj. “Instantaneous Load-Based User Association in Multi-Hop IAB Networks using Reinforcement Learning”. In: *GLOBECOM 2020 - 2020 IEEE Global Communications Conference*. 2020, pp. 1–6.

[42] Sergey Shaboyan, Alireza S Behbahani, and Ahmed M Eltawil. “Practical Considerations for Full Duplex Enabled 5G Integrated Access and Backhaul”. In: *Journal of Signal Processing Systems* (2020), pp. 1–10.

[43] Goksel Simsek, Hande Alemdar, and Ertan Onur. “Multi-Connectivity Enabled User Association”. In: *2019 IEEE 30th Annual International Symposium on Personal, Indoor and Mobile Radio Communications (PIMRC)*. 2019, pp. 1–6.

[44] Meryem Simsek et al. “IAB Topology Design: A Graph Embedding and Deep Reinforcement Learning Approach”. In: *IEEE Communications Letters* 25.2 (2021), pp. 489–493.

[45] Cristian Tatino et al. “Maximum throughput scheduling for multi-connectivity in millimeter-wave networks”. In: *2018 16th International Symposium on Modeling and Optimization in Mobile, Ad Hoc, and Wireless Networks (WiOpt)*. 2018, pp. 1–6.

[46] Fasil B Tesema et al. “Mobility modeling and performance evaluation of multi-connectivity in 5G intra-frequency networks”. In: *2015 IEEE Globecom Workshops (GC Wkshps)*. IEEE. 2015, pp. 1–6.

[47] Oumer Teyeb et al. “Integrated Access Backhauled Networks”. In: *2019 IEEE 90th Vehicular Technology Conference (VTC2019-Fall)*. 2019, pp. 1–5.

[48] Bangzhao Zhai et al. “Mesh Architecture for Efficient Integrated Access and Backhaul Networking”. In: *2020 IEEE Wireless Communications and Networking Conference (WCNC)*. 2020, pp. 1–6.

[49] Hongtao Zhang, Wanqing Huang, and Yi Liu. “Handover probability analysis of anchor-based multi-connectivity in 5G user-centric network”. In: *IEEE Wireless Communications Letters* 8.2 (2018), pp. 396–399.

[50] Xiaoqian Zhang, Fangfang Liu, and Hailun Xia. “Ergodic Capacity Analysis for Full-Duplex Integrated Access and Backhaul System”. In: *2019 IEEE Global Conference on Signal and Information Processing (GlobalSIP)*. 2019, pp. 1–5.